The bright outburst of a new black hole candidate: Optical observations of MAXI J1820+070 from the Montsec observatory.

Engineering Physics: Bachelor Thesis

Grau en Enginyeria Física: Treball de fi de grau

Barcelona, October 2019

Author: Carlos Celma Querol [1,2]

Advisors: Manuel Linares [1] & Dave Russell [2]

1: Universitat Politècnica de Catalunya (UPC)
2: New York University Abu Dhabi (NYUAD)

Abstract

The motivation of this thesis is to monitor the data of the 2018 outburst of the black hole candidate MAXI J1820+070. This project combines theoretical background about X-ray binaries with the experimental work done in the process of achieving optical magnitudes using a CCD camera: Telescopi Joan Oró ground based telescope.

We present the optical light curves and colours of MAXI J1820+070 during the March-November 2018 outburst. After obtaining the magnitudes, using MAXI and Swift-UVOT as space observatories we extend our range to the X-ray band and study the different states and physical processes that occur in them.

Finally, we give physical interpretation of all obtained data and characterize the spectral shape of the infrared, optical, UV and X-ray emission in the different components of MAXI J1820+070 outburst.

We conclude that MAXI J1820+070 show the typical properties of a BHT: our results show the canonical BHT states, the disk irradiation changing in the soft state and the linear increase of the R-I colour indicating a cooling of the disk. We also give evidence that the optical emission in the soft state is bluer than in the hard.

Contents

List of figures

List of tables

CHAPTER 1. Introduction

1.1 X-ray binaries

Binary systems consist of two stars orbiting around a common centre of mass. More than half of the stars in our Galaxy are expected to be in binary or multiple systems (Zurita et al. 2012). In this project we focus on X-ray binaries (XRBs). XRBs are formed by two stars; one is a normal star typically in the main sequence, and a compact object: a neutron star or a black hole.

In the 1960s bright X-ray sources were discovered and in consequence several models trying to explain these sources were proposed. This helped prove the existence of neutron stars and black holes as compact objects.

After that in 1971 the Uhuru satellite clarified that the production of X-ray luminosity was linked with the release of gravitational potential energy of the mass transferred.

According to the mass of the companion star we can divide them in two groups:

- High-mass X-ray Binaries (HMXBs).
- Low-mass X-ray Binaries (LMXBs).

	X-ray Spectra	*Time variability*	*Optical Counterparts*
HMXBs	Relatively hard. $kT \geq 15\ keV$	Regular pulsations.	Massive companion. ($M > \sim 5\ M_{\odot}$)
LMXBs	Soft. $k\,T \sim 5 - 10\ keV$	X-ray bursts with quasi periodic oscillations.	Low mass companion. ($M < \sim 3 M_{\odot}$)

Table 1.1. Characteristics of HMXBs and LMXBs. Credit: King et al. 2002

But not all HMXBs and LMXBs have the same properties, for example black hole LMXBs do not produce X-ray bursts.

As their name describes, XRBs release X-ray radiation with wavelengths from 0.01 to 10 nm. In fact, they are many orders of magnitude more luminous than the Sun in X-rays, but not especially bright compared to many other stars at optical wavelengths. XRBs, according to their changes in brightness, are

classified as persistent or transient. The process that powers an XRB is called accretion: matter falls onto the compact object, releasing large amounts of energy at the expense of its gravitational potential energy.

Persistent XRBs are always accreting; they can have variations in the emitted flux, but by less than three orders of magnitude. On the other hand, transients show a wider range of X-ray luminosities. We can quantify this saying that in transients the optical and X-ray luminosity increase by a factor 10^3-10^6 during their outbursts.

The X-rays are created in the area around the compact object where the material of the companion star is falling and it reaches temperatures closer to one million degrees, in the innermost parts of the accretion flow.

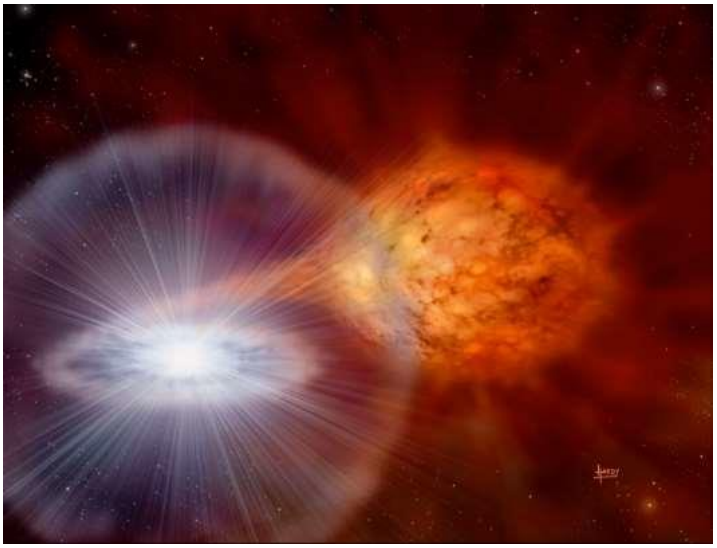

Figure 1.1 Artistic image of the accretion process. We can see the companion star (orange), and the compact object which is accreting its mass. Moreover, the wind produced by both is appreciable in the image. Credit: Astrophysics Group Southampton University.

The accretion process in XRBs (Figure 1.1) is different if we consider HMXBs or LMXBs systems. In HMXBs the companion stars are bright in optical range and are of early spectral type usually, O or B, their accretion is achieved by winds. On the other hand, LMXBs were the first extrasolar X-ray sources discovered. In LMXBs matter is accreted via an accretion disk. The mechanism of Roche Lobe Overflow explains how the accretion and the disk is achieved in LMXBs.

The components, leaving aside the compact object, of these systems are:

- Accretion disk: The inner part is very hot and releases UV and X-ray radiation. In general, we can detect them due their high temperature. We also have evidence of a hard X-ray emitting region sometimes called corona whose geometry is a topic of debate.
- Secondary star: Typically, it is very faint and cool, and we are not able to detect it in many LMXBs in outburst since the emitted optical radiation by the disk outshines the companion star. We expect a low-mass and likely evolved star.
- Jet: It is an astronomical event that takes place when ionised matter is focused in an extended beam along the axis of rotation. The jet usually appears in the hard state and we expect radio emission from it.
- Corona: Whose geometry is debated. The corona is known to be the part between the compact object and the innermost part of the disk. It has an important weight in the hard state where the disk is truncated far from the hole. In this state, it likely emits hard X-rays. Contrary to that, in the soft state when the disk approaches the compact object the corona can merge with it. That results in the loss of the capacity of emitting hard X-rays.

The region where the flow is gravitationally bound to a star is the Roche lobe. The gravity of the compact object pulls the mass of the companion star. When it leaves the companion's Roche Lobe and enters that of the compact object a disk is created. The angular momentum prevents it from being captured directly and as a result we get the accretion disk mentioned (see again Figure 1.1). We call the point that joins both Roche Lobes the inner Langranian point of the system.

In the accretion disk, we find several orders of magnitude in temperature which are present because inner parts near the compact object are hotter than the outer ones. This implies that we can consider the total disk as the sum of infinite rings with each ring having different temperature.

Gravitational potential energy is the main source of energy. Because the material in the disk experiences differential rotation, friction between inner parts of the accretion disk releases radiation. The loss of energy implies that matter approaches the innermost part of the disk and finally it falls. This explains how a LMXB outburst is powered. The luminosity of the LMXB depends on the mass accretion rate, the mass and the radius of the compact object which is given by:

$$L_{acc} \approx \dot{M}\frac{GM_{CO}}{R} \sim 10^{37}\ erg\ s^{-1}\ (1.1)$$

With a typical mass accretion rate of $\dot{M} \sim 10^{17}\ g\ s^{-1}$

Moreover, the orbits of the flow in the disk are circular and with velocity $v(R) = \sqrt{\frac{GM_{CO}}{R}}$ (1.2) depending on R as the position of the flow element observed , we can neglect the self-gravity produced by the disk as its density and total mass is much lower than the compact object. The mechanical energy of an orbiting flow element is:

$$E_{\Delta M} = \frac{1}{2}\frac{GM_{CO}\Delta M}{R}\ (1.3)$$

Adding all flow elements in the disk and computing their total luminosity:

$$L_{Disk} = \frac{1}{2}\frac{GM_{CO}\dot{M}}{R} = \frac{1}{2}L_{Acc}\ (1.4)$$

Meaning that the other half of L_{acc} has still to be released very close to the compact object. So, half of the energy is radiated in the disk due the friction that flow makes when it spirals inwards, and the other half is released when flow reaches the compact object.

1.2 Black hole transients

In this section we focus on transient X-ray binaries where the accreting compact object is a black hole. These systems are called black hole transients (BHT). They are useful because we can determine the masses of the system components knowing their velocities, so they are a powerful tool to obtain black hole masses and study accretion processes.

Throughout the last half century several black hole candidates in XRBs have been detected: Only, 18 stellar-mass black holes have been confirmed and they are all in XRBs. We have other 37 potential candidates showing similar spectral properties to be confirmed. The estimation of the number of XRBs in the Galaxy is about 10^4, but only 1300 are expected to be detectable as BHTs (Corral-Santana et al. 2015).

BHTs experience several states during the outburst (more detailed discussion in the next section) with typical luminosities between 1-100% of the Eddington's value (Soleri 2010).

The Eddington's luminosity from the spherical accretion is the maximum luminosity that the system can produce. This value is achieved when the pressure produced by the emitted light expels the mass that would otherwise fall onto the compact object. After that, accretion is slowed but the compact object is emitting less light since it receives less mass. So, the light's pressure drops, accretion accelerates and reaches again Eddington limit.

After such accretion episodes also, also known as 'outbursts', the system luminosity decays for several weeks or months and remains in quiescence from years to centuries (Casares 2010).

1.3 Accretion states

The behaviour of a BHT can be characterized in terms of spectral states and transitions between them. These states are defined considering the X-ray variability and spectral properties showed by the sources during their outburst phases. We can represent them in a hardness-intensity diagram (HID) (Figure 1.2) where the X-ray count rate is plotted as a function of the X-ray spectral hardness (chapter 3). States do not have a universally accepted physical origin, but their definition is useful to understand the changes in the accretion flow. The main states during the outburst of a BHT are:

- Quiescence: Matter transferred from the companion star accumulates in the outer disk and is redistributed by viscosity. Even though the mass accretion rate in the innermost regions is very low, the mass transfer rate through the inner Langranian point may continue unaltered.

- Low-Hard State (LHS): Takes place typically at the beginning and at the end of an outburst. It corresponds to the right nearly-vertical branch in HID. The X-ray spectrum is hard, shaped by the inverse Compton effect (Gilfanov 2010). Namely, hot electrons transfer their energy to photons.

- Hard-Intermediate State (HIMS): Associated with the horizontal branches in the HID. It comes after the initial LHS and before the final LHS, can also be present in central parts of the outburst but in short periods of time. Energy spectrum is softer than in the LHS. We can also have quasi-periodic oscillations (Motta et al. 2015).

- Soft-Intermediate State (SIMS): When hardness and variability amplitude drop below a certain threshold, the source enters the SIMS. The energy distribution is like the HIMS, but the properties are different: the band-limited noise disappears and is replaced by a power-law noise.

- High-Soft State (HSS): The leftmost branch in the HID. We have a soft spectrum, with an important thermal disk contribution. A hard component is detected with oscillating intensity. This state encompasses a larger range of luminosity values but not as large a range as the hard state.

When a black hole emerges from quiescence it releases a considerable amount of hard X-ray radiation (hard state), and then evolves into a softer X-ray spectrum which is due to the geometrically thin accretion disk, which extends very close to the black hole. It is not fully understood how this transition is completed, but drastic physical changes apply to the disk and the corona.

We have evidence suggesting that the corona is compact, and the disk can extend close to the central black hole (Belloni et al. 2011). We also think that the accretion disk in the hard state is truncated at a few hundreds of the Schwarzschild radius[1] from the black hole. The process of truncation occurs when the inner disk radius is far from the black hole.

In summary, we can say that a BHT outburst follows the same trend, it goes from low to high luminosity and does the main hard-soft transition at higher luminosity than the soft–hard transition. This phenomenon is known as hysteresis. This can be observed in figure 1.2 starting from quiescence and moving along the diagram anticlockwise, we characterize all state transitions. The loop can be completed within 1 week to 1 year (Muñoz-Darias et al. 2011).

1 The Schwarzschild radius is defined as $R_s = \frac{2GM}{c^2}$ where G is the gravitational constant, M is the object mass, and c is the speed of light.

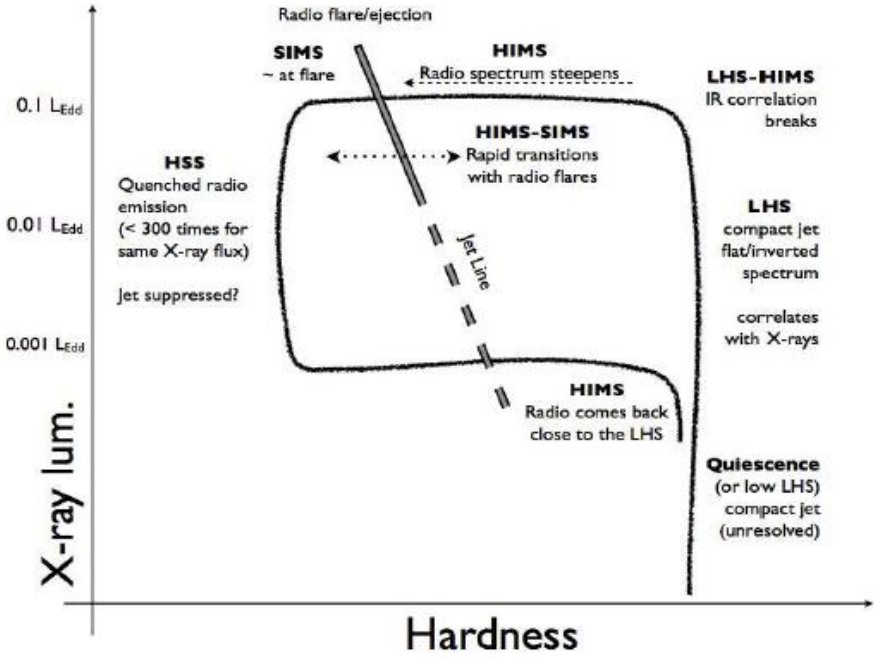

Figure 1.2. Stylised Hardness-Intensity diagram of a black hole transient Credit: T. M. Belloni, S. E. Motta and T. Muñoz-Darias 2011

1.4 MAXI J1820+070

On March the 11th, 2018 a new X-ray source was discovered at the coordinates (R.A., Dec) = (275.112 °, 7.037 °). After the detection of this new X-ray transient by the Japanese mission MAXI (Chapter 3) (Kawamuro et al. 2018), the source was named as MAXI J1820+070. Telescopes around the world observed it, and detected strong emission in optical and radio.

Baglio et al. 2018 detected the optical counterpart on March 14th, 2018. The source was too bright in X-ray to be considered as an accreting white dwarf and its distance was not allowing it to be a neutron star binary (Russell et al. 2006). After that, the first outburst ended in the last week of October.

We know that MAXI J1820+070 is at about 3 kpc (Gandhi et al. 2018), but the mass of the companion and the black hole are not known. We may be able to calculate these when the system is in quiescence, with optical spectroscopic observations of the companion star.

On March the 9th 2019, MAXI J1820+070 had an unexpected rebrightening in optical band and it was confirmed by Baglio et al. 2019. Between the 9th and the

11th March 2019 its V luminosity increased from magnitude 17.2 to 15.4 that means the second outburst has not been so luminous as the first when the peak magnitude in V band was almost magnitude 13. Finally, this second outburst ended at the beginning of May 2019 when its rate decay increased from 0.06 mag/day to 0.19 mag/day (Zampieri et al. 2019).

This was expected since the secondary outburst is always fainter than the main (Muñoz-Darias et al. 2016). But the typical quiescence time is of the order of some dozens of years, and this secondary outburst has taken place in less than a year.

Then, in August after some months in quiescence (V magnitude of 18.3) MAXI J1820+070 brightened progressively to a V magnitude of 15.9 throughout the 12 days before the 7th August 2019 (Hambsch et al. 2019).

We have monitored the source over nine months with the Joan Oró Telescope at the Montsec Observatory (Chapter 4). We also accessed the Swift-UVOT data (Chapter 5), so we have been capable to gather both information to study the IR-optical-UV emission of MAXI J1820+070 during its main 2018 outburst. Using MAXI observations, we characterize its X-ray emission and accretion states (Chapter 3).

CHAPTER 2. Observations and data analysis

After the introduction chapter, we focus on how the data were obtained (facilities and instrumentation used) and the different procedures done (data reduction and analysis) to extract the desired magnitudes. For this and the next chapters DS9 has been used as the software to display astronomical images.

2.1 Observatori astronòmic del Montsec

The observations that we have used were taken from the Observatori Astronòmic del Montsec (OAdM). This is a scientific facility built and managed by Institut d'Estudis Espacials de Catalunya (IEEC) with the economic support of the Catalan Government.

It is in the Montsec Mountains, at a height of 1570 m. Since it is far from crowded cities, avoiding pollution and light, it is considered an excellent site for astronomical observation.

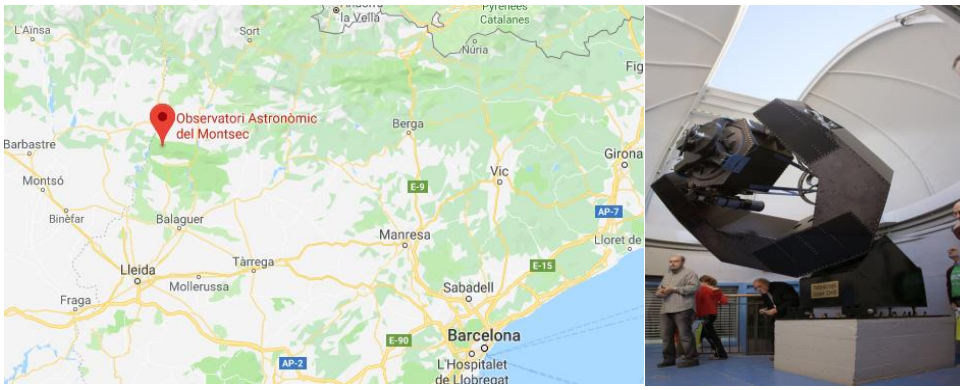

Figure 2.1 (Left) Map showing the location of OAdM: Montsec Mountains, 50 km north of the city of Lleida in the municipality of Sant Esteve de la Sarga. (Right) Picture of the Telescope Joan Oró. Credit: The map has been grabbed from google maps & the TJO telescope is an image from Jordi Payá.

Three main telescopes and a camera to detect dangerous near-Earth asteroids form the OAdM. The three telescopes are:

- Telescopi Joan Oró (TJO). With a diameter of 0.8 m it is one of the most important facilities used in this project (see next section). Since the 26th of November 2018, it has a new CCD camera. It belongs to Catalan Government, but it is controlled by the IEEC.

- Telescopi Fabra-ROA Montsec. This telescope has a diameter of 0.5 m and it regularly does surveys about the quality of the sky, and can also detect

and follow near-earth objects. It is owned by the Reial Acadèmia de Ciències i Arts de Barcelona and the Real Observatorio de la Armada.

- XO-Montsec. It is used for the XO project which searches extrasolar planets around bright stars. Besides the Montsec unit, there are two more identical units cooperating with the project; one in Canary Islands and the other in Utah. Each unit of the telescopes consists of two Canon lenses of 0.1 m diameter. The telescope belongs to the Space Telescope Science Institute, USA.

Several institutions are concerned about the correct operation of the OAdM and also participate in an active way in its maintenance. Including the Universitat Politècnica de Catalunya (UPC).

2.2 Telescopi Joan Oró

TJO is the only OAdM telescope used in our project. Operated since 2007 by the IEEC, was the motivation for the construction of the OAdM in 2004. Nowadays TJO is still the largest Catalan telescope, with a 0.8m diameter, named Joan Oró after the Catalan astrobiologist. It works normally in a fully automated way, but it can be set in a manual mode. For our observations it used the MEIA 2 camera (see next section) as its main instrument. Software architecture is needed in order to control the observations and the robotic dome. The system is managed by OpenROCS which is a software created to control observatories.

Potential observers must send their proposals and a committee will evaluate which of them are the most suitable to award observation time.

2.3 The MEIA2 CCD camera

The MEIA2 instrument is the tool that we used to obtain images throughout our observation campaign. It consists of two components: the CCD camera and the filter wheel, which is physically coupled to the telescope. It can hold up to 12 filters of size 3-inch that are placed at the optical axis of the telescope.

The CCD camera is an Ikon L, with a chip manufactured by Andor. Table 2.1 shows some relevant specs of MEIA2:

Model	CCD42-40
Sensor Manufacturer	E2V
Sensor Type	Back Illuminated
Number of pixels	2048x2048
Pixel Size	13.5x13.5 μm
Field of view at TJO	12.3x12.3 arcmin
Peak Quantum Efficiency	96%
Typical Working Temperature	223 K
Typical Gain	1.05 e^-/count
Typical Dark Current	<1 e^-/(pixel*s) at 223 K
Typical Read Out Noise	9 e^- RMS at 3MHz
Read-out time	10 seconds

Table 2.1. MEIA2 camera principal specifications. From: http://www.ieec.cat/en/content/229/meia2

While observing, photons reach the pixels of the CCD. But the camera cannot read this photon counts. It must convert them into an electric current which is the physical parameter that can be measured. The table above indicates the most important specifications for the photon/current conversion. Two of them are:

The peak quantum efficiency which its percentage shows the detected photons that finally can be converted into a current. We also have the readout gain which is given by the chip that reads the current: 1.05 e^-/count in this case. It means that the camera produces 1 count for every 1.05 recorded electrons. Without knowing the gain, a number of electron counts is meaningless.

2.4 Data reduction

This section explains the steps followed to analyse all available TJO data. All the sections refer to the March-November 2018 data obtained from the TJO telescope using the MEIA2 camera. Our data were obtained using Ultraviolet (U), Blue (B), Visible (V) (Johnson), Red (R), Infrared (I) (Cousins) filters in the filter wheel.

That means a set of 16457 images distributed in 113 nights and in the 5 Johnson-Cousins filters. (See Table 1 on appendices).

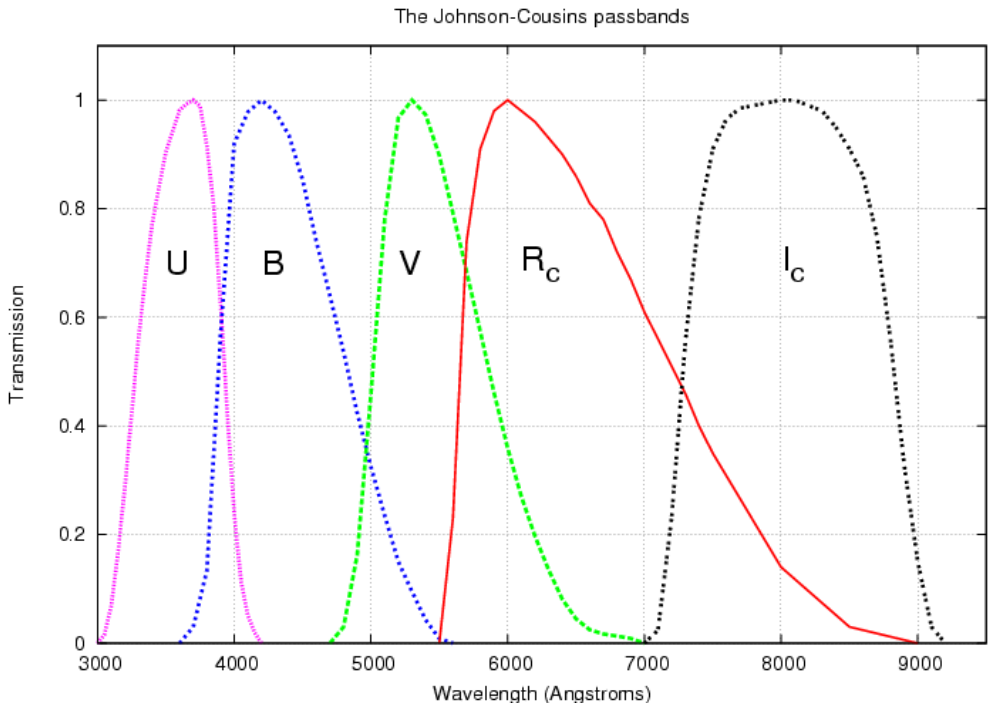

Figure 2.2. Johnson-Cousins filters transmission profile. Note that the central wavelength does not coincide with the peak of transmission. Credit: Tabalweh et al. 2018.

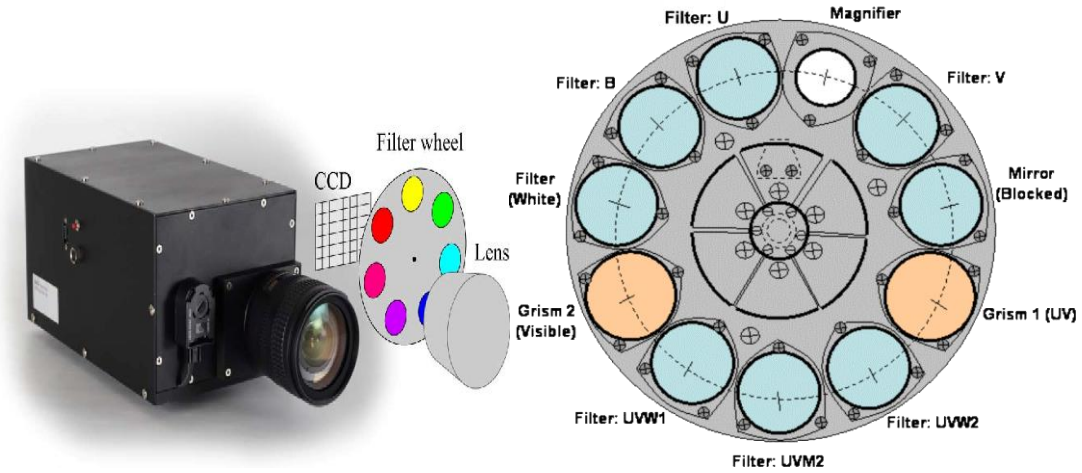

Figure 2.3. (Left) Profile of a camera filters wheel and showing its position. Credit: Brauers et al. 2008. (Right) UVOT filter wheel sketch. Credit: https://www.mssl.ucl.ac.uk/www_astro/uvot/uvot_instrument/filterwheel/filterwheel.gif

2.4.1 Calibrations: bias, flat & dark

Our first step was to download the data from the Montsec observatory webpage. The images downloaded could be raw (with no treatment) or reduced (with treatment that we explain below).

The raw images are the natural images that the camera captures. Some corrections applied later guarantee that raw images have the best precision: bias, dark and flat field (explained below). When a raw image undergoes these three corrections it is converted into a reduced image.

- Bias: The camera has a base level of read out noise. Bias correction removes the unwanted noise that is produced by sensors in the effect of reading the main signal.

- Flat: This correction is applied to be sure that all pixels give the same result of counts when exposed to the same quantity of light. Dust motes or lens flaws may create the effect of bad pixels or sensitivity differences across the pixels, with this correction we can correct for such imperfections.

- Dark: After a long exposure, camera components will be hotter than at the beginning of the observation session since the number of thermal counts is proportional to the exposure. This is going to introduce thermal noise; its level is affected by the temperature, exposure time and the light sensitivity of the camera.

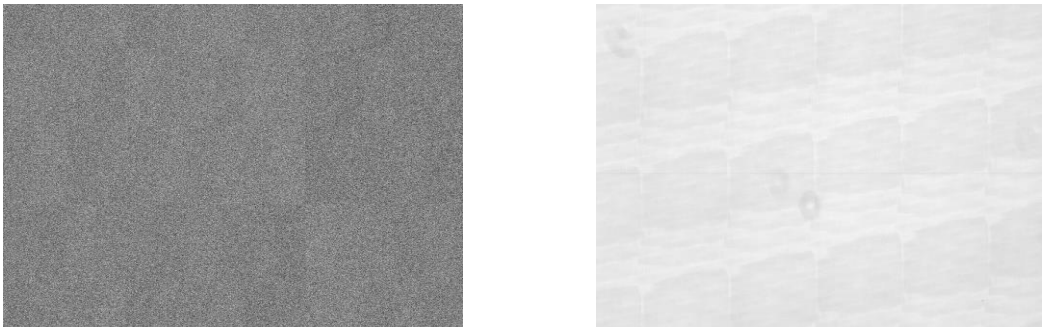

Figure 2.4. (Left) Bias Frame. (Right) Flat Frame. Note that we can see some slight imperfections in the flat frame image.

All calibrations were performed to increase the signal precision. The frames to apply the corrections were also supplied by the OAdM webpage.

To summarize we can say that this equality holds:

$$Reduced\ image = \frac{Raw\ image - Dark\ Frame}{Flat\ Field\ Frame}$$

Where the bias frame has been subtracted previously from all raw frames of observation (science) and flat/dark images.

To perform these corrections, we used IRAF (Image Reduction and Analysis Facility) a collection of software geared towards the reduction of astronomical images.

We took the raw images of the 27th May 2018 and after applying all calibrations, we compared our results (the result in each filter) with the reduced by the TJO pipeline. The images agreed better to than 5%. Thus, we conclude that the TJO pipeline provides reliable calibrated products.

2.4.2 Averaging

After checking that the calibrations applied to the raw image yield the desired result, we use the reduced ones for each night. We have more than one frame per night and per filter, so in order to improve our signal to noise ratio we combine these images. After combining the frames, we end with a single frame per night and per filter. To achieve the combined frames, we used IRAF with the imcombine function (see Table 1 in appendices), the total full TJO dataset that we have analysed occupies 273.5 GB of hard disk space (tar version).

Another important parameter in the images was the exposure time, with range between 1 and 30 seconds the images with high exposures give better signal to noise ratio.

To apply imcombine we run the command in IRAF. Imcombine takes an input list of images, does the average of the images and returns the combination of all in an output image. An offset in world coordinate system is applied before averaging. That means that the task can correct for pointing drifts. This is very important to avoid blurred or duplicated stars in the average images.

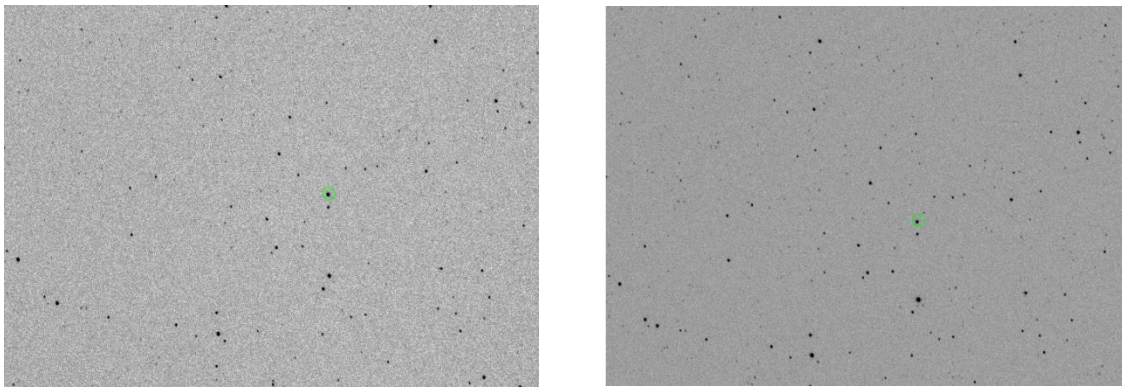

Figure 2.5. (Right) A combined image ready to be used to extract data. (Left) One of the images used to perform the combination. Note that the combined image is clearer, meaning better signal to noise ratio. The green circle shows the location of MAXI J1820+070.

Then we checked if all new images were suitable to perform aperture photometry. We removed the ones that were not able to give us enough precision, basically images where no stars are detected since their bad signal to noise ratio. The problem with these images could be low exposure time or the seeing.

2.4.3 Alignment of the images

After the combined images are obtained, we must align them to be used in the Ultracam software (see next section).

Ultracam goes through a list of images and extracts the counts of the desired targets. The point is that Ultracam does not detect the world coordinate system (fk5) but the coordinates are affected by the pointing drifts (physical coordinates).

The process of shifting images can be done basically by using the imshift task in IRAF. Imshift task grabs a list of images and applies a desired shift to them. We calculate the desired shift using ds9's ruler.

First, we choose a night as a template and identify the desired sources by selecting them. Then, we save these regions in physical coordinates. Now, we can open them in another image. Calculating the difference in both axes, we find the shift that the image needs to overlap with the previous. Repeating this process for each night we finally ended with all the images aligned to be entered in Ultracam.

2.4.4 Aperture photometry (Ultracam)

The objective of the aperture photometry is to estimate the magnitude of a given source analysing the current measurements of the CCD camera (see MEIA2 instrument section).

After detecting MAXI J1820+070 in our field of view, we choose two reference stars (details are given in the next section). The reference stars are necessary to determine how the seeing and the atmosphere turbulence is affecting the source's light. The goal is to compare MAXI J1820+070 to the reference ones and check how they change throughout the observation nights. Moreover, it helps to remove other sky effects such as the airmass of the target, elevation or the apparition of thin clouds.

To continue we had to convert the fits format image (typical in astrophysics image) into a ucm format, which is used by the Ultracam software. The steps followed by Ultracam are: look for the centroids (central point of the star, where it is brightest), fit a point spread function to measure the seeing, set an extraction radius for the source, the reference stars and the sky annulus, and finally find net counts (figure 2.6).

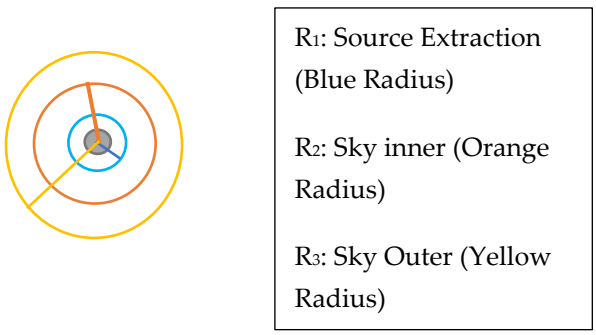

Figure 2.6. Sketch of an Ultracam procedure. The grey is the source that we are observing, blue is the circle whose radius is used by Ultracam to extract number of counts. Orange and red circles radius are used to obtain a sky annulus and know the background intensity.

Ultracam finds the centroid of the grey source as an example, we show an idealized sketch in figure 2.6, calculating the center of the bright distribution. Then fits a point spread function (PSF) (in our figure 2.6 represented by the grey circle).

After setting the extraction radius R_1 considering the seeing, Ultracam calculates two values: the photon counts that reach the blue circle with radius R_1 and the

sky (background) counts estimated using an anular region of radii R_2 and R_3. Then, net counts are obtained subtracting this background level from the total counts.

These steps are performed with the task 'reduce'. To perform the reduction, we must give to Ultracam a text file containing a list of the ucm files that are going to be analyzed. Once given the list ultracam goes through each image extracting the counts, errors and positions.

To begin our analysis, we must choose an aperture (Figure 2.7). This must be done using the setaper task and choosing one of the ucm images as the template. The apertures function is to indicate where is each star that we want to extract counts in each frame. It also has a tool to mask close stars if their shining might affect our source. Another important function is to link our stars to the brightest in our field of view, this helps the program to identify where are our stars.

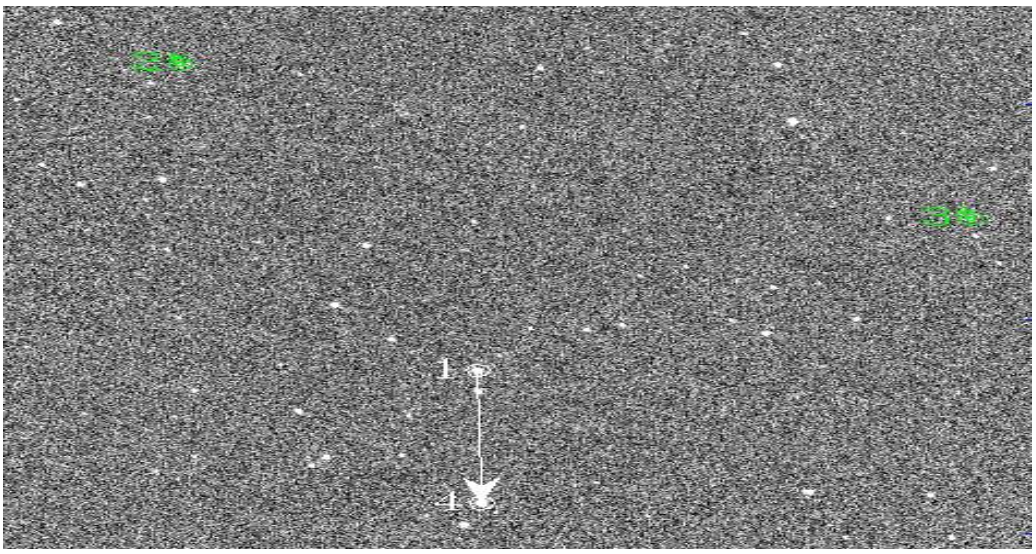

Figure 2.7. Aperture scheme used to perform the aperture photometry with Ultracam. '1' is our science target, '2' and '3' are the reference stars (left and right in table 2.3, respectively) '4' is the brightest star in our field of view.

In the aperture we also set the reference stars, shown in green in figure 2.7. Note that in the image (Figure 2.7) our source was linked to the brightest star in the field, this helps the software to correct the previous mentioned pointing drifts.

2.4.5 Reference stars

To complete aperture photometry we must choose some reference stars. We use the APASS catalogue, after introducing the coordinates of MAXI J1820+070 and search in a 0.2 arcmin radius in it, we receive a list of the most suitable stars to be chosen; that is stars relatively closer in our field of view, visible in all bands and with known magnitudes (similar to the target) and errors. The candidates cannot exceed the maximum counts allowed by each pixel of the camera; we refer this as unsaturated stars. Finally, two reference stars were chosen (see Table 2.2).

	LEFT REFERENCE STAR	**RIGHT REFERENCE STAR**	
RA (°)	275.13	275.03	
Dec (°)	7.113	7.150	Averages
U (Mag)	15.56±0.04	14.96±0.03	15.26±0.03
B (Mag)	13.65±0.05	13.56±0.05	13.60±0.03
V (Mag)	12.27±0.06	12.39±0.06	12.33±0.04
R (Mag)	11.50±0.07	11.77±0.08	11.63±0.05
I (Mag)	10.585±0.188	11.01±0.20	10.96±0.14

Table 2.2. Magnitudes of the reference stars (B, V, R, I) extracted from APASS catalogue. The U magnitude has been calibrated using UVOT data (see UVOT section for more information).

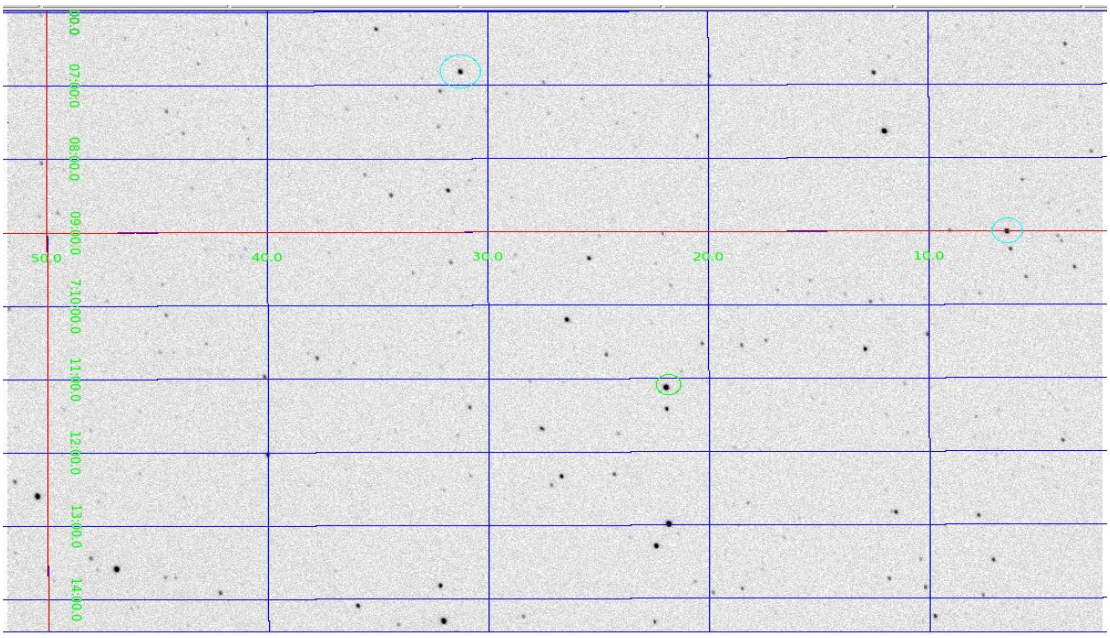

Figure 2.8. Image showing the position of the reference stars, circled in cyan. MAXIJ1820+070 is marked in green.

2.4.6 Magnitude & flux calibration

After performing the aperture photometry, we obtain as a result a text file that contains the most important parameters to be considered in our study. The relevant information for us are the counts of our source and of the reference stars, after the sky background has been taken in account (that means subtracted of the total counts).

So finally, we obtain the counts of our source for each day. With that we can obtain the differential magnitude:

$$\Delta m = -2.5 log \frac{T}{S} \qquad (2.1)$$

Δm is the differential magnitude. T is the number of total source counts subtracting the background (net counts) and S is the average of the net counts of the two reference stars.

Since we have two reference stars, we calculate the average of their net counts (S). However, the error in the counts is present so we use the propagation error formula to find the error on the differential magnitude:

$$\varepsilon_{\Delta m} = \sqrt{\Sigma \left|\frac{\delta f}{\delta x}\right|^2 \varepsilon_x^2} \quad (2.2)$$

Where x means each independent variable

After all calculations the final formula is:

$$\varepsilon_{\Delta m} = \frac{2.5}{\ln(10)} \sqrt{\frac{\sigma_L^2 + \sigma_{Lsky}^2 + \sigma_R^2 + \sigma_{Rsky}^2}{\left(L - L_{sky} + R - R_{sky}\right)^2} + \frac{\sigma_T^2 + \sigma_{Tsky}^2}{\left(T - T_{sky}\right)^2}} \quad (2.3)$$

Now, we have obtained the differential magnitude with its error. To convert it into the final apparent magnitude we used the average magnitude of both reference stars and added it to the differential magnitude.

Once we have the magnitudes, we can convert them to a flux (F_m). To do this we use the formula with zero points (F_{zp}):

Considering that a flux is proportional to its source counts and applying the definition of magnitude, we get for every filter:

$$m_1 = k - 2.5log\frac{F_1}{t} \quad (2.4)$$

$$m_2 = k - 2.5log\frac{F_2}{t} \quad (2.5)$$

Where k is a constant depending on the filter, m and F are the magnitudes and the fluxes and t is the interval of time in which the flux has been measured (Bessell 2005). Subtracting both equations, we get:

$$m_1 - m_2 = -2.5log\frac{F_1}{F_2} \quad (2.6)$$

Considering that the zero-point flux $\left(F_{zp}\right)$ that is associated to a magnitude m=0, yields:

$$m = -2.5log\frac{F_m}{F_{zp}} \quad (2.7)$$

Finally, we get:

$$F_m = F_{zp} * 10^{\frac{-m}{2.5}} \quad (2.8)$$

Where m is the reddened magnitude, F_m is the flux associated to that magnitude and F_{zp} is the zero-point flux which depends on the used filter (see Table 2.3).

Applying the error propagation formula, we obtain the error in the flux:

$$\varepsilon_{Fm} = \frac{ln\ 10}{2.5} * F_m * \varepsilon_m \quad (2.9)$$

Where ε_{Fm} is the flux error and ε_m is the magnitude error.

The zero-point fluxes are:

Filter	**Central Wavelength (nm)**	**Zero Point Flux (Jy)** [2]
W2	192	738
M2	224.6	771
W1	260	891.5
U (TJO) / U (UVOT)	365.6/346.5	1823 / 1441
B	435.3	4130
V (TJO) / V(UVOT)	547.7/546.8	3781/ 3646
R_c	634.9	2941
I_c	879.7	2635

Table 2.3. Zero-point fluxes and central wavelengths of optical and UVOT filters. Credit: UBVRI filters zero points have been extracted from Cohen, Walker, Barlow, and Deacon, 1992; http://www.swift.ac.uk/analysis/uvot/filters.php ; https://www.aip.de/en/research/facilities/stella/instruments/data/johnson-ubvri-filter-curves.

With all this we are able to calculate the fluxes needed. (See Table 2 and 3 on appendices).

[2] Jansky is a flux density unit. 1 Jy=10^{-23} $\frac{erg}{s\ cm^2\ Hz}$

2.5 Swift-UVOT photometry

TJO dataset gives an excellent coverage of the outburst decay, but it hardly covers the rise. In order to study the outburst rise and extend the spectral energy distribution (explained in the next chapters) to the far UV range, we analysed the available Swift-UVOT dataset on MAXI J1820+070. See UVOT dataset in appendices.

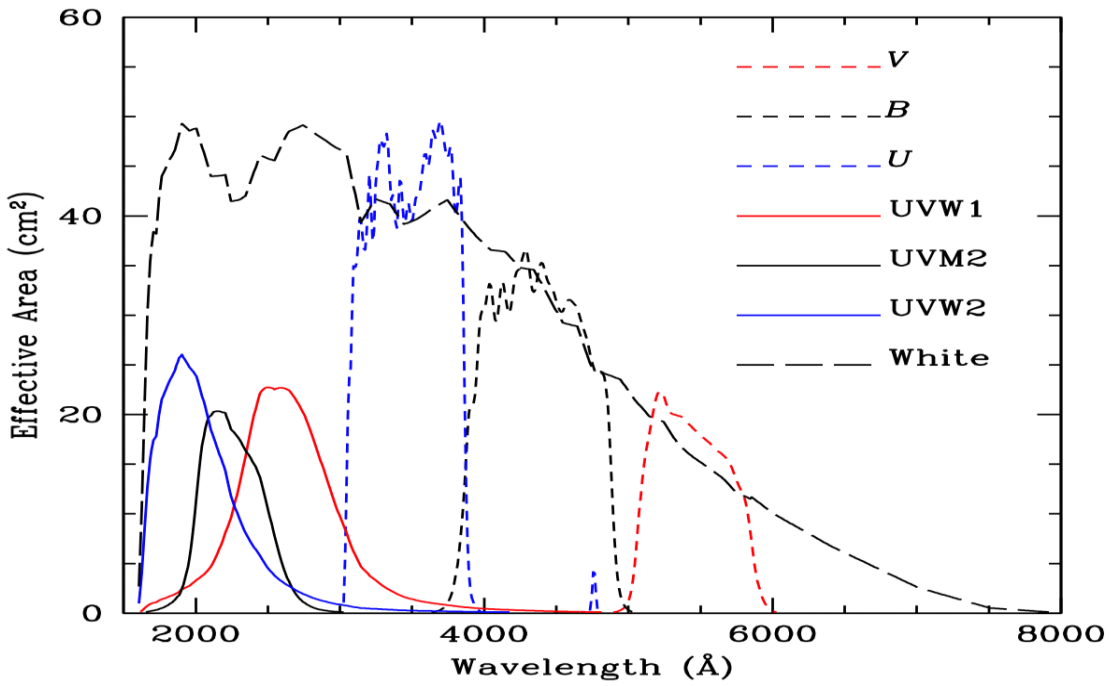

Figure 2.9. UVOT profile of transmission filters. Credit: http://www.swift.ac.uk/analysis/uvot/filters.php

Swift is a multi-wavelength observatory dedicated to study gamma-ray burst science. It is focused on energy bands higher than the optical such as gamma-ray, X-ray and UV bands. Since its reliability, these measurements are of interest for the astronomical community and all data is processed and uploaded by NASA as soon as possible. It possesses different telescopes coupled with itself. For our analysis we analyse data from UVOT.

The Ultraviolet and Optical Telescope (UVOT) is one of the telescopes onboard the Swift satellite. It is a 30 cm diameter, sensitive to magnitude 22.3 in a 17 min exposure.

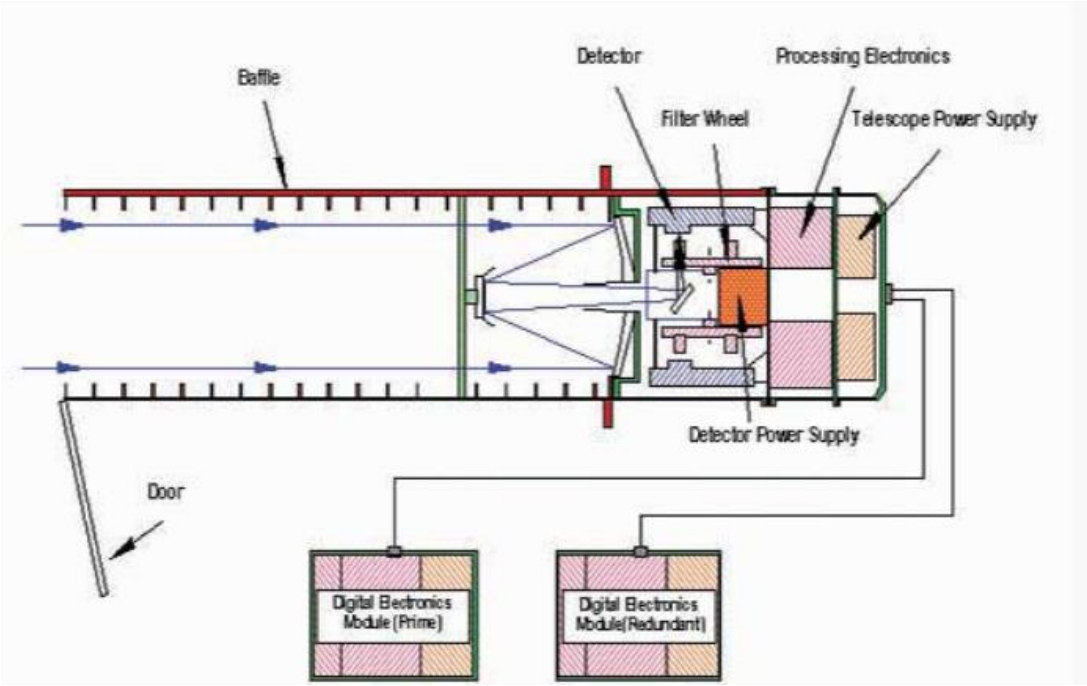

Figure 2.10.. Configuration of an UVOT layout. Credit: https://swift.gsfc.nasa.gov/about_swift/uvot_desc.html

2.5.1 Swift-UVOT data reduction

For the Swift-UVOT reduction we use Heasoft. Heasoft has Swift-UVOT specific tasks which are able to calculate the magnitudes and fluxes of the stars in a given image.

After all Swift-UVOT data available of MAXI J1820+070 were downloaded, we could proceed with the analysis.

We added all the images from the same observation and filter. Using the 'uvotimsum'[3] task. This is performed to increase the signal to noise ratio. The next step is to perform the aperture photometry. This is achieved using the 'uvotsource'[4] task. In this case we used a circle of 6.1 arcsec radius for both. The

[3] *uvotimsum infile=uvot_images outfile=output_image method=GRID exclude=none. Where the infile and outfile are the images that uvotimsum must be applied and the result respectively.*

[4] *uvotsource image=input_image srcreg=source.reg bkgreg=bkg.reg sigma=3 apercorr=CURVEOFGROWTH cleanup=yes chatter=1 outfile=uvotsrc_results.fits > uvotsrc_results.txt*

source region returns the UVOT system magnitudes if the aperture corrections (apercorr) are set in curveofgrowth. The background region must be placed away from contaminating light sources in order to know which level is detected when no stars are present.

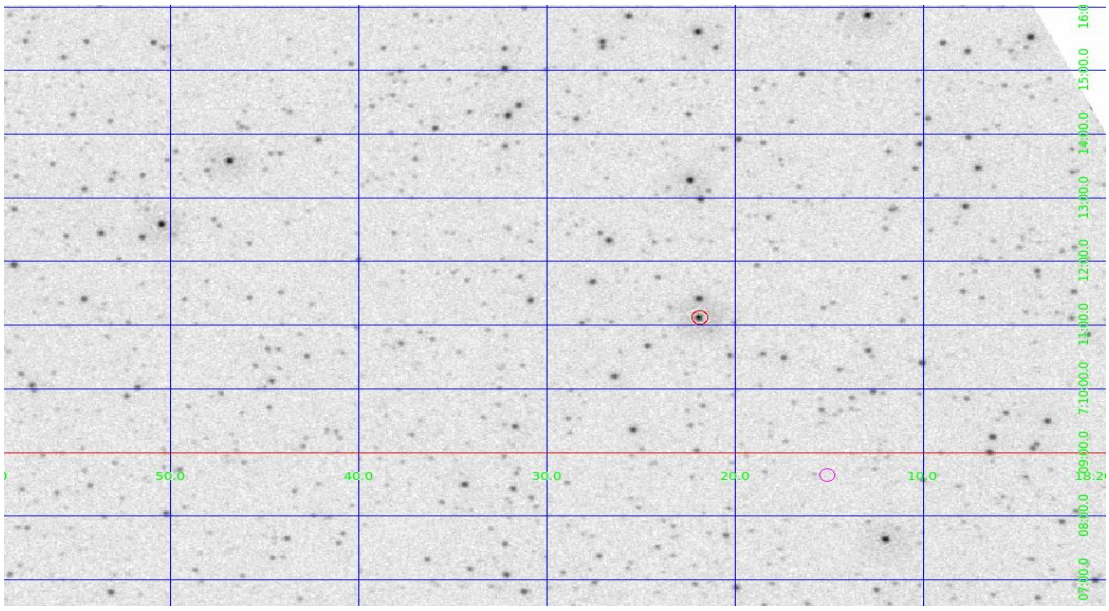

Figure 2.11. Source (red circle) and background (magenta circle) regions. We are seeing a UVOT image in U filter.

With this analysis we obtain magnitudes and flux densities for each UVOT observation. (See Table 4 and 5 on appendices).

2.6 Extinction

The extinction is the absorption and scattering of the electromagnetic radiation by interstellar dust and gas particles between an astronomical object and the observer. This can be measured from the hydrogen column density (see Figure 2.12). Since blue light is more attenuated than the red, objects are seen redder than they are, due to this fact sometimes extinction is called reddening.

Let A_v be the difference (extinction) between the source V magnitude after going through the interstellar medium (m_v) and the V magnitude that we would percept us if no dust was present (m_{v0}).

$$A_V = m_v - m_{v0}$$

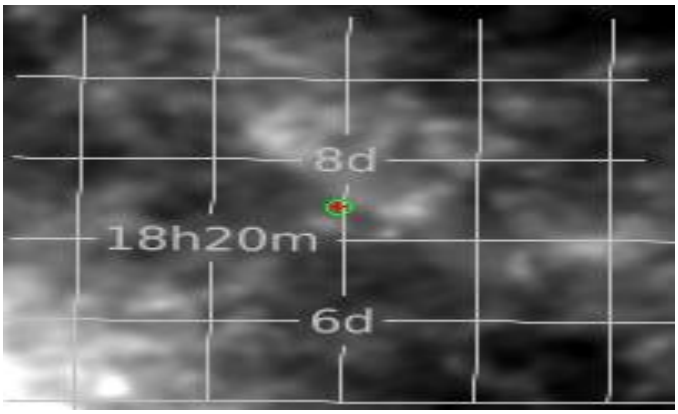

Figure 2.12. Dust Map around MAXI J1820+070.This dust can be approached by a hydrogen column density. Credit: Caltech

We assume dust to gas ratio constant $N_H = 1.12 * 10^{21}\ cm^{-2}$ (Fitzpatrick 1999) and $\frac{N_H}{A_v} = 2.87 * 10^{21} \pm 1.20 * 10^{20}\ cm^{-2}\ mag^{-1}$ (Foight et al. 2016). That yields an A_v=0.390 mag.

Once we know the $\frac{N_H}{A_v}$ ratio, the extinction values for the optical filters (from U to I) are taken from (Fitzpatrick 1999). UVOT extinction coefficients were calibrated using (Mathis et al. 1990). We use A_v to obtain the reddening coefficients in all bands.

Table 2.4 shows are the extinction values applied to obtain reddened magnitudes:

Filter	Extinction (Mag)
W2	1.046±0.057
M2	1.140±0.062
W1	0.825±0.045
U	0.596±0.032
B	0.516 ± 0.027
V	0.384 ± 0.021
R	0.310 ± 0.017
I	0.183 ± 0.010

Table 2.4. Reddening coefficients of all bands used Credit: Fitzpatrick et al. 1999 & Mathis et al. 1990.

Mathis coefficients take in account the absorption dip in filter M2. For this reason, we get a higher extinction than W2. This is unexpected because W2 band is bluer and we expect larger extinction than M2.

CHAPTER 3. X-ray states & hardness-intensity diagrams

In this chapter, we present the X-ray properties of the 2018 outburst of MAXI J1820+070 and discuss them in the context of the known accretion states from BHTs. Analysing the data obtained from MAXI telescope we characterize the X-ray radiation emitted by MAXI J1820+070. The hardness-intensity diagram explained in chapter 1 can be plotted by means of our data and be adapted to MAXI J1820+070.

When we talk about X-rays, we refer to the range of energies from 0.1 to 100 keV. That means they are more energetic than UV but not as much as gamma rays. We can classify them in hard X-rays with energy above 10 keV or soft if their energy is below. However, this threshold varies in the literature. Now, we explain which equipment is used to perform the detection in X-rays.

Monitor of All-Sky X-ray Image (MAXI) (Figure 3.1) uses several equipment to detect X-rays. Some of its components are a gas slit camera and another based on solid-state physics. Due to its design, MAXI is continuously observing all the sky: every 96 minutes it scans the sky. Thanks to this, we have been able to improve our knowledge about black hole candidates, X-ray flares and binary X-ray pulsars. MAXI is coupled to a module of the International Spatial Station and was developed by the Japanese Aerospace Exploration Agency (JAXA) in Tsukuba, Japan. MAXI observed MAXI J1820+070 daily.

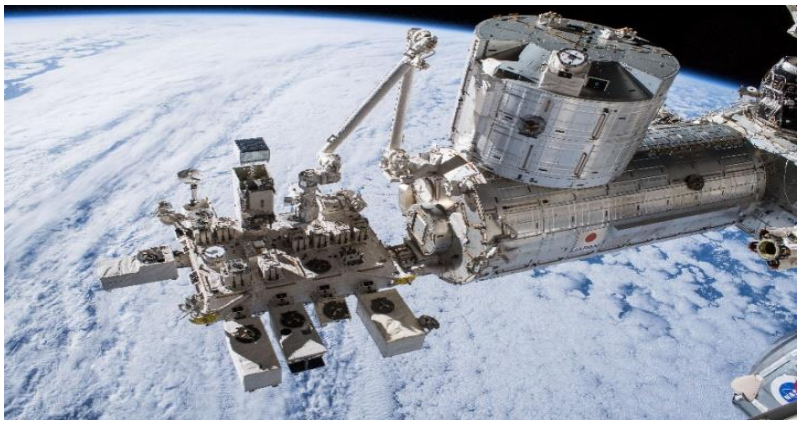

Figure 3.1. Japanese Experiment Module (JEM) Pressurized Module (JPM) and Japanese Experiment Module - Exposed Facility (JEM-EF) with the Earth in the background. Taken by Expedition 55 crew. MAXI has been attached in this module Credit: NASA Image: ISS055E006395NASA

3.1 X-ray light curve

X-ray light curve measure the number of photon counts that reach the detector of MAXI per unit time, over the course of several months. MAXI detects the photons in the 2-4 keV, 4-10 keV and 10-20 keV energy bands. We can add the 2-4 keV band with 4-10 keV one to finally obtain the intensity in the 2-10 keV band (Figure 3.2), which covers the whole range of soft X-ray radiation. Thus, this radiation is emitted during the soft and hard state, so it is useful to compare variations.

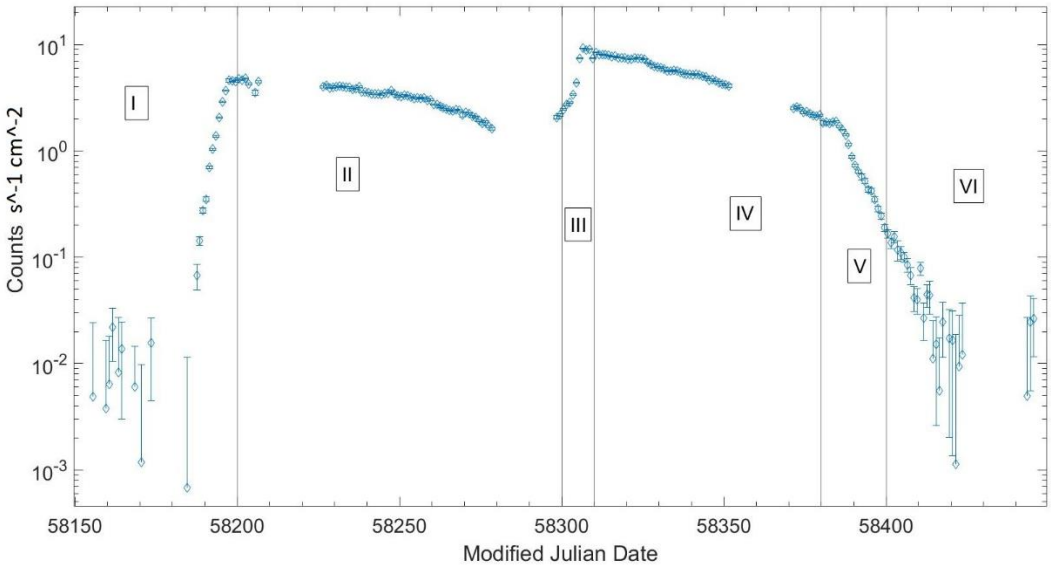

Figure 3.2. X-ray light curve (2-10 keV). X axis shows the lapse of time between March and November 2018. Y axis is in logarithmic scale and shows the counts per second and per square centimetre between (2-10 keV) in logarithmic scale.

After seeing the X-ray light curve (Figure 3.2) the hardness ratio explained in the next Section, we can clearly differentiate six stages along the outburst:

Stage I (58150-58200): At the beginning of our observations (before MJD 58200), the X-ray intensity is increasing. This is known as the outburst rise. The peak around MJD 58200 indicates the end of the initial rise (as we will see in the light curves).

Stage II (58200-58300): Then, a smooth decay is observed in the hard state and finishes near MJD 58300. That is when starts the hard to soft state transition. (see hardness on Figure 3.3)

Stage III (58300-58310): Just before MJD 58300, a rebrightening is seen linked with hard to soft state transition. Note that this peak in MJD 58308 is higher than

the previous one. However, we are showing 2-10 keV band and from MAXI data we can justify that radiation in 10-20 keV band is a factor 2.5 higher in the first peak. In the soft state luminosity is usually larger than in the hard, but in the hard state the emitted radiation is harder.

Stage IV (58310-58380): After this second peak, we observe a smooth decay of about one order of magnitude again until MJD 58380. MAXI J1820+070 is in the soft state.

Stage V (58380-58400): Then this smoother pattern is changed by a steeper decay, this is the soft-hard transition, as the signature of entering the hard state again after MJD 58400. In this abrupter decay, the 2-10 keV counts diminish more than an order of magnitude.

Stage VI (58400-58430): After 58400, a steeper decay trend is continued. MAXI J1820+070 is again in the hard state. This final stage (VI) is similar as the initial (I), we can see the data being affected by considerable errors associated with the hard state variability and the low X-ray flux.

3.2 X-ray hardness

Hardness is used to refer to the energy of the X-rays, a harder radiation thus is a more energetic than a soft (see last section on chapter 2). We present the results of the hardness ratio, which we define as the intensity in the bands $\frac{4-10\ keV}{2-10\ keV}$, during the days of the observation from MJD 58150 to 58450, to avoid shown fluctuations in the error at the beginning and the end of the outburst seen in figure 3.2. We plot only the MAXI data where the value of the points is larger than the errors associated with them. In figure 3.3 we can plainly see the trend followed by the hardness.

We can match the X-ray light curve discussed in the previous section with the hardness evolution. An approximate ratio value of 0.43, leaving aside the scatter, is observed during (I), (II) and (VI). On the other hand, in the soft state the hardness ratio (IV) starts at 0.13 and follows a linear decay falling to a value of 0.08.

From the hardness ratio we can detect state transitions at first sight. As said in the last section, hard to soft transition (III) was reported by Homan et al. 2018 between MJD 58296 and 58304. From figure 3.3, the following information is extracted:

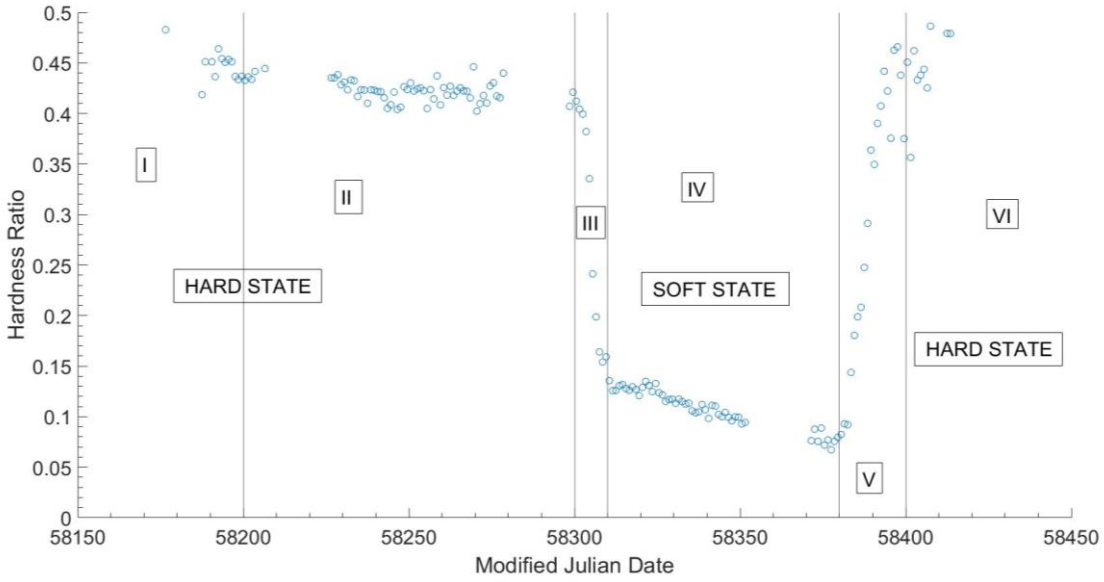

Figure 3.3. Evolution of MAXI J1820+070's hardness ratio (4-10 keV/2-10 keV) during the outburst.

The hard to soft transition starts on MJD 58301.5 with a hardness ratio of 0.40 and finishes in MJD 58311.5 with a value of 0.13, that represents a decay in the hardness of 0.03 units per day. On the other hand, the soft to hard state transition starts on MJD 58382.5 (V) with a value of 0.09 and finishes on MJD 58409.5 (VI) with a value of 0.51, that yields a rise rate in the hardness of 0.02 per day. So, the rise rate is slightly inferior to the decay one. Note that after the soft to hard transition we end with a slightly larger value (0.51) than in the initial hard state (0.45).

At the other state transition (soft to hard) reported by Motta et al. 2018: according to the observations of MAXI team, the source again rapidly transitioned to the hard state on 58383 or shortly before, consistent with the spectral change detected between 58382 and 58384 (V).

3.3 Hardness-intensity diagram

The Hardness-Intensity diagram (HID) is a powerful tool to see the evolution of the X-ray hardness and the luminosity of the source throughout the outburst days. Figure 3.4 shows the HID of MAXI J1820+070.

In our diagram (Figure 3.4) we can distinguish different areas: the right-bottom part associated with the hard state (the outburst begins from here), the central part which is associated with intermediate states and the left-top one which corresponds the soft state.

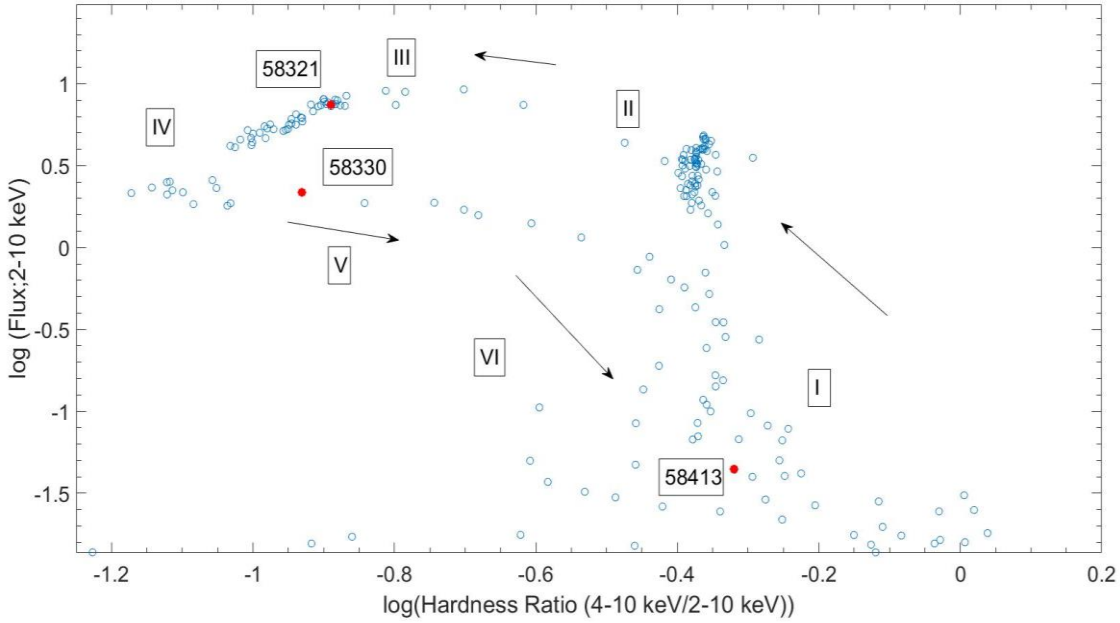

Figure 3.4. Hardness-Intensity diagram of MAXI J1820+070. The arrows show the evolution of the outburst. Moreover, the red points show some MJD during the loop.

The outburst process that follows MAXI J1820+070 is starts in the right-lower (hard state) part, the rightmost vertical branch represents this outburst rise. Then enters in the intermediate states (up horizontal branch) and goes though until reaches the leftmost vertical branch. This branch corresponds to soft state and its luminosities are larger than in the hard state as we can see in the diagram. MAXI J1820+070 completed this loop in 343 days, since the first date in the diagram is the MJD 58188.5 and the last is MJD 58531.5. Note that the zones with larger accumulation of points belong to slower states and vice versa in the emptier ones.

From it, we select some days to build diagrams showing the flux profile in different effective frequencies, known as spectral energy distribution. These diagrams will be useful to see if the spectral index (slope of the spectral energy distribution) changes in the state transitions (Chapter 6).

CHAPTER 4. Optical and near-infrared emission

In this chapter we present the results obtained using the procedure explained in chapter 2, focusing on magnitudes obtained using the Joan Oró Telescope. We analyse images taken with the UBVRI filters, which span the wavelength range from 365.6 nm (ultraviolet) to 879.7 nm (near-infrared).

4.1 Light curve

We present our results in light curve form: a plot showing the magnitude of MAXI J1820+070 versus the time of observation measured in Modified Julian Date (MJD). Figure 4.1 shows the apparent magnitude in the UBVRI set of filters. The X axis covers the range from 58150 to 58450 MJD, which corresponds to February 2nd to November the 28th, 2018. The Y axis indicates the magnitude value. It is important to remember that the definition of magnitude implies that lower values are brighter, and vice versa.

Therefore, we are going to interpret how the light curves and the optical colours change as a function of the states explained in chapter 1 with the behaviour of MAXI J1820+070 shown in these graphics (see next figures). In the next figures, we present the results for each magnitude in Johnson-Cousins filters (detailed information about these filters is given in Chapter 2).

Merging all the bands, we obtain the final TJO light curve:

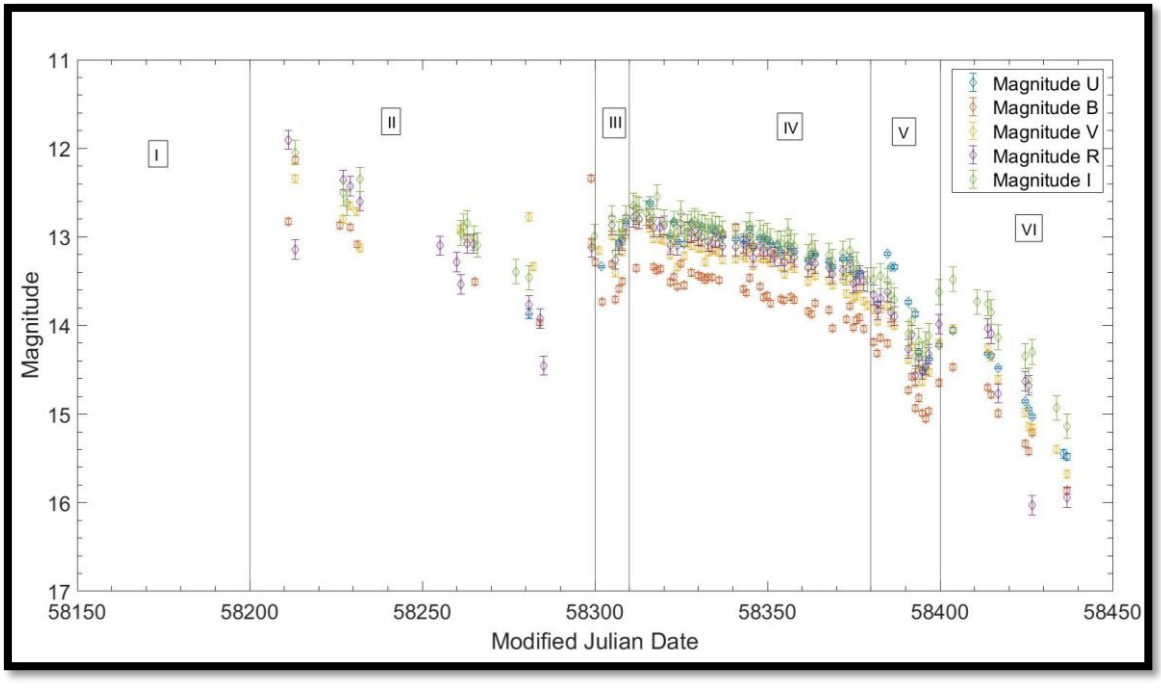

Figure 4.1. Light curve of MAXIJ1820 with all (U,B,V,R,I) TJO bands.

From the final light curve and comparing it with the X-ray states/hardness, we can extract the following information:

At the beginning of the outburst (initial rise) (stage I) no data are available from TJO observations. After that (II), following the typical BHT evolution, the source flux decays while staying in the hard state. It then experiences a hard to soft state transition around MJD~58300 (III); exactly between 58300 and 58310 in MJD. This transition shows a clear brightening in the optical (TJO) bands. It is interesting to note that the X-ray variability frequencies (in particular, that of the frequency QPO) started increasing 4 days before (on MJD 58296 according to Homan et al. 2018, ATel 11820).

Then, in the range of 58310<MJD<58380 (IV): we classify this region as the soft state. During this state the light curve looks smoother. The peak magnitude is in MJD 58316 with a value of 12.69±0.14 mag in the I band. The lowest value is found close the transition to hard state in MJD 58385 (V) with a value of 13.50±0.14 mag also in I band. Between these two points a smooth decay rate of 0.1 magnitude per week is observed.

The last period of our analysis 58400<MJD<58450 (VI) corresponds to the hard state again. We can clearly see a dip and then a rise in all bands with magnitude B of 15.05±0.03 with MJD 58396, corresponding to the transition from the soft to the hard state (Figure 4.1).

4.2 Optical-near infrared colours

Once we obtain the magnitudes, we calculate colours. Colours are useful to give physical interpretations about light emission and relate them with the BHT state, they can also be used as an estimate of the system's temperature. They are obtained subtracting two chosen magnitudes, depending on which are chosen different kind of information may be extracted. In this section we display the colours calculated using TJO observations (Figure 4.2). We have chosen the following data:

- B-V colour = Magnitude B – Magnitude V
- R-I colour = Magnitude R – Magnitude I

We can only do these subtractions when in the same MJD both magnitudes are available (observed).

This choice of colours is useful because we are taking neighbour bands in the set UBVRI, indicating changes in the emission of close wavelengths. That can be the result of changes in the physical properties of the jet and/or the accretion disk.

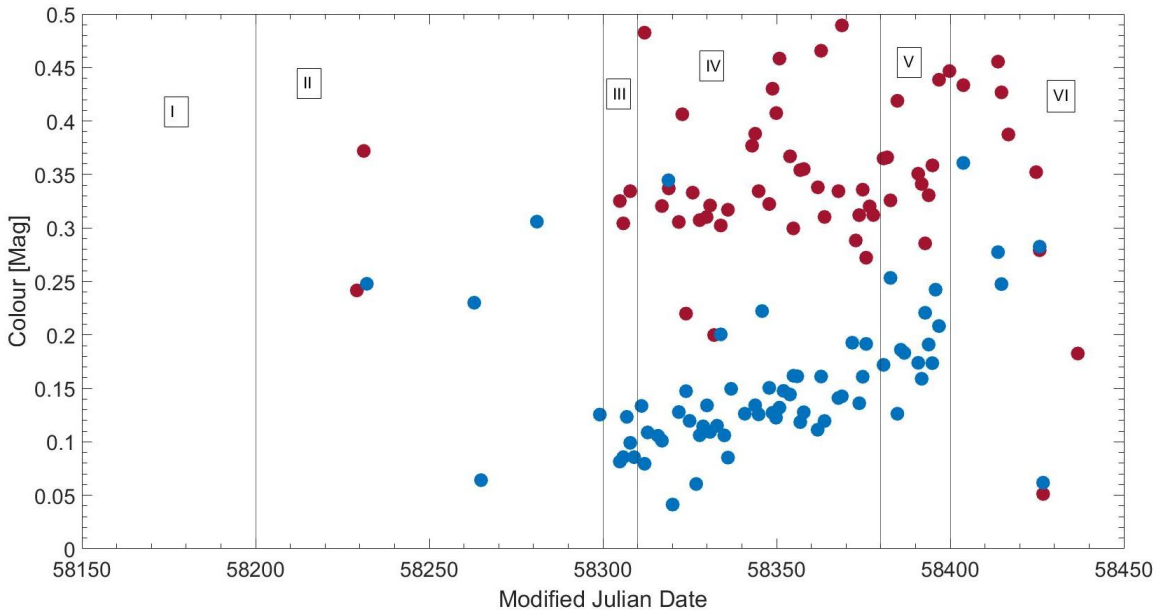

Figure 4.2. (Red Circles) B-V Colour & (Blue Circles) R-I Colour of MAXI J1820+070. Note the increase in R-I colour in the soft state (IV).

We present our colour plots in scatter form. It is important to say that the R-I colour scatter average error is 0.17 mag so that dominates the scatter, nevertheless we can distinguish a trend. On the other hand, the B-V colour shows a quite lower average error of 0.06 mag.

For our sampling of MAXI J1820+070, we have observations allowing us to calculate 60 days for B-V colour and 75 for R-I between the range of MJD from 58213 to 58437.

In the soft state, the SED has a positive spectral index, $\mu \approx 1$ (see Chapter 6) and it is thought that most of the optical radiation is produced by reprocessing in the accretion disc (like other XRBs; e.g. Hynes 2005). There is no evidence for jet emission, and this is only expected in the hard state. The light curve (Figure 4.1) is decaying smoothly.

The trend in B-V colour seems to be a flat line fluctuating around 0.3 mag, except perhaps a peak near MJD 58350 with a value less than 0.1 magnitude in difference with the other data. After the transition to the hard state, MAXI J1820+070 becomes bluer due to the rise on the B-V colour. On the other hand, the R-I colour

shows a clear increasing tendency with a value of 0.014 mag/week going from ≈ 0.1 on MJD 58300 to 0.2 near MJD 58400. The increase of R-I colour indicates a decrease of the system temperature (discussed in chapter 6). This linear increase of the R-I colour is one of the main results of this project.

CHAPTER 5. Ultra-violet emission

In this chapter, we explain the results obtained using UVOT data. We present these results in the form of light curves and colour evolution, like in Chapter 4. The X axis in the plots covers the same range of MJDs (see introduction in Chapter 4).

5.1 Light curve

We present our UVOT light curve (Figure 5.1). We can see that the state transitions (around MJD 58300 and 58400) between these states are smoother than in the TJO optical light curve.

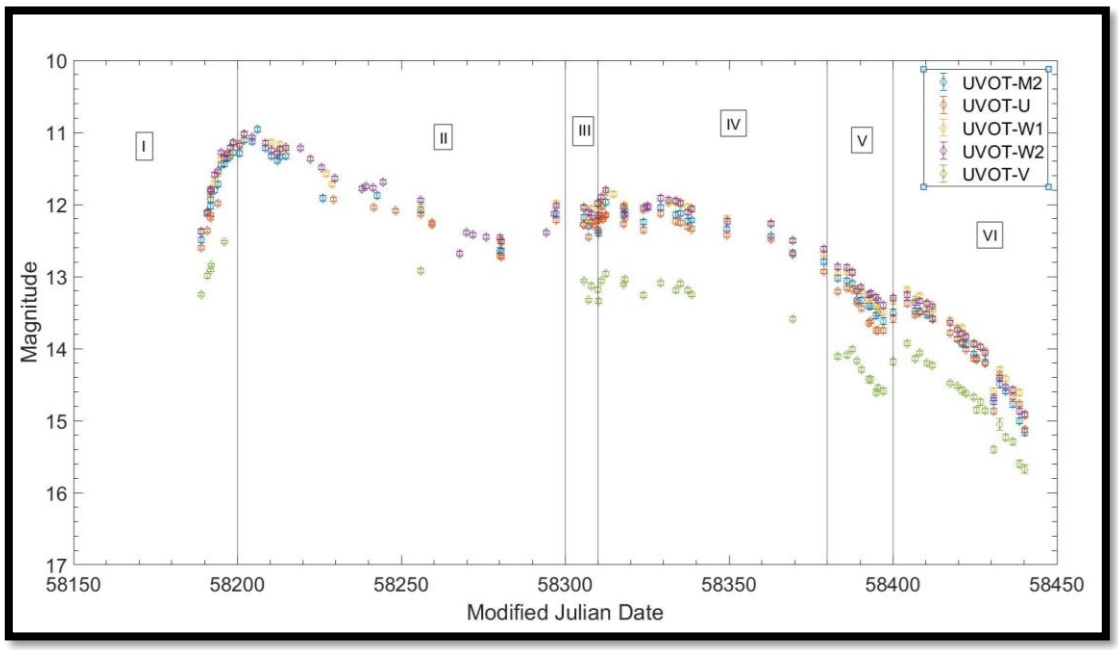

Figure 5.1.UVOT (M2,W2,W1,U,V) light curve.

From the UVOT light curve we can see: a peak magnitude is reached in MJD 58204 (II) with a magnitude of 11.0 in the W2 band, then a smooth decay until MJD 58300 (III). When it enters the soft state, the source brightness by 0.2 mag between MJD 58297 (II) and MJD 58310 (III). Then the source starts to decay again until MJD 58400 (V), where we find a dip and then rise in all bands.

5.2 Optical-near ultraviolet colours

We have calculated W2-I colour and we have plotted data from last chapter (V-I and I-R colours) to have a point of reference to compare with. All colours are shown in Figure 5.2:

- V-I Colour = Magnitude V- Magnitude I

This colour is a good estimation of the change in the ends of the optical filters range associated with TJO observations. The behaviour is the expected, showing fluctuations of around 1 mag in the initial state (I, II). Then a monotonic almost flat line is observed in the soft state (IV). In the soft to hard transition (V) we observe a rise of 0.5 mag indicating that the emission of light has become bluer (VI).

- W2-I Colour = Magnitude W2- Magnitude I

W2-I colour is the difference between the reddest filter (I) and the bluest one (W2). That approximates the behaviour of the whole detected spectra. It remains constant during almost of all the soft state (IV), we can see perhaps a rise of 1.15 mag in the change to the soft state (transition) in MJD 58300 (III) then suddenly experiences a dip stopping the decreasing at 0.35, after the dip in all bands (MJD 58400) it rises from -1 mag to -0.5 mag (VI). We can see that this colour is very sensitive to state transitions.

- R-I Colour = Magnitude R- Magnitude I

R and I are close filters, so we are analysing local changes in the SED. The colour seems to have high variability during the initial stage (II) and then stabilizes at the beginning of the soft state in MJD 58300 (III, IV). After the soft to hard transition (MJD 58400) fluctuations of around 0.5 mag are observed (VI), like in the previous case. This colour is dominated by large scatter errors around 0.15 mag, as mentioned in the previous chapter.

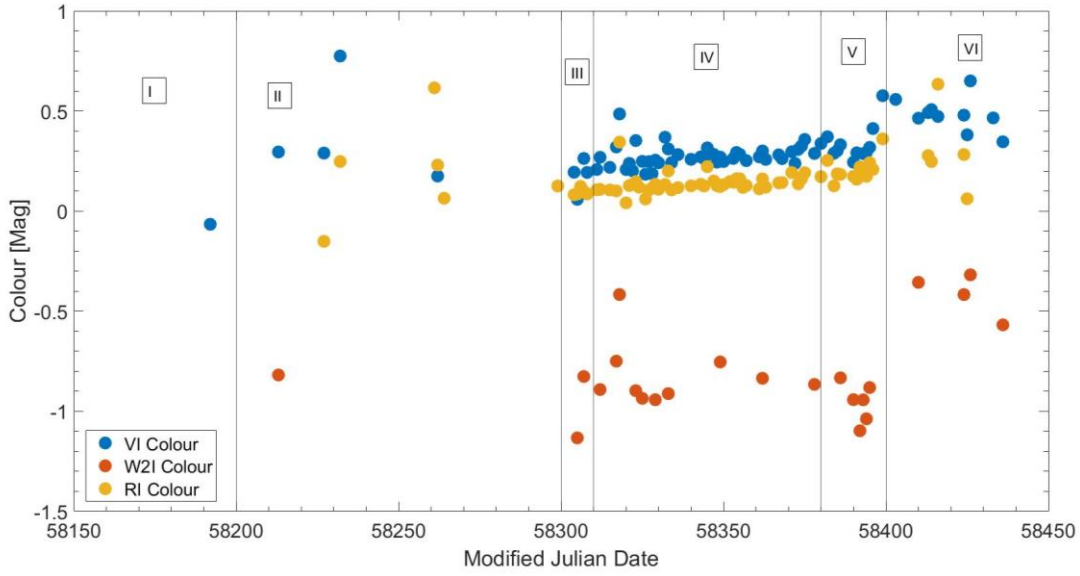

Figure 5.2. UVOT colours of MAXI J1820+070. In red circles W2-I colour, blue V-I colour and yellow R-I colour.

5.3 Comparison between UVOT&TJO in the shared bands

In this section we discuss the results obtained in the same filters in TJO and UVOT; these results are the U and V band. Note that we are talking about same bands because they are referred as U and V in both cases. However, they are not equal because UVOT and TJO use filters with a slightly different central wavelength (Table 2.3). Omitting this slight difference, it is useful to check if there are important differences to detect mistakes in the calibration of any of the light curves.

After seeing the plots (Figure 5.3, Figure 5.4) we can say that the TJO&UVOT bands agree with each other. In V band we can see that both telescopes observations overlap each other, as expected for similar zero points.
On the other hand, U band looks shifted. We can relate this difference with the zero points and assuming that the final flux is the same in both bands:

$$F_{TJO} = F_{UVOT} \quad (5.1)$$

$$F_{zpTJO} * 10^{\frac{-m_{TJO}}{2.5}} = F_{zpUVOT} * 10^{\frac{-m_{UVOT}}{2.5}} \quad (5.2)$$

First, isolating and defining $dm = m_{UVOT} - m_{TJO}$ and then, using the flux zero points in chapter 2, we obtain $dm = 0.26\ mag$
In these calculations we have not considered the dereddening because we use the same extinction value in both cases (0.596±0.032).

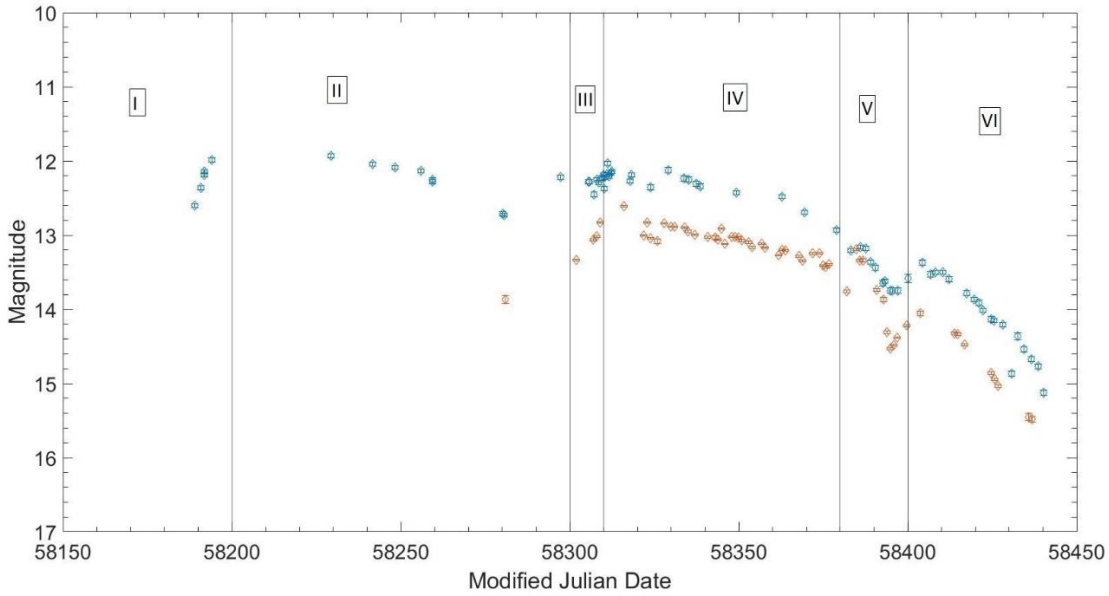

Figure 5.3. U band comparison TJO (orange) & UVOT (blue).

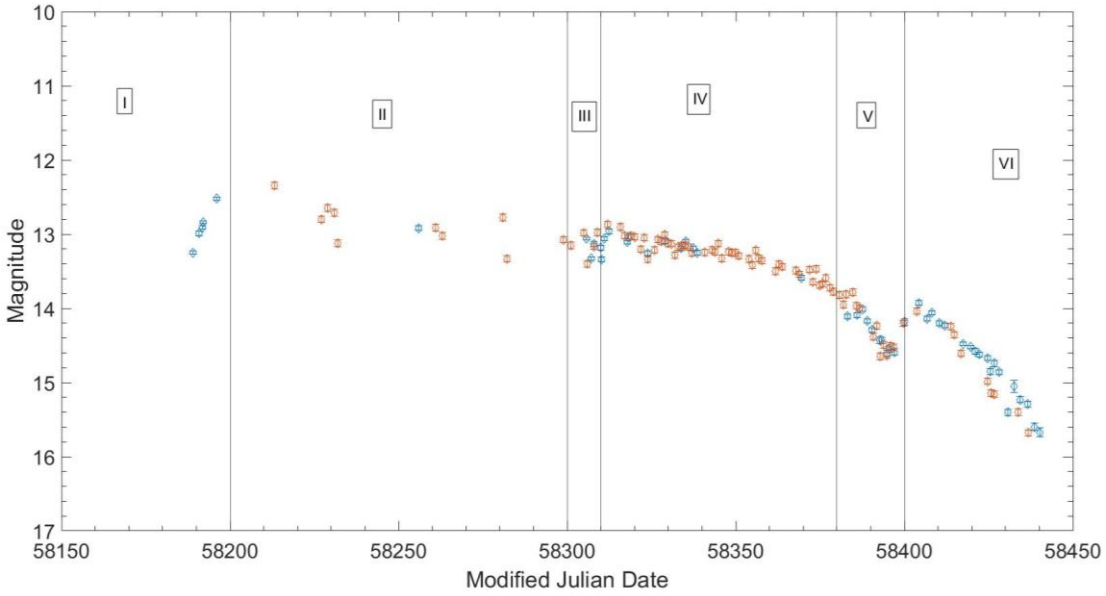

Figure 5.4. V band comparison TJO (orange) & UVOT (blue).

CHAPTER 6. Broadband Spectral Energy Distribution

After obtaining all magnitudes and fluxes, we investigate and present the spectral energy distribution (SED), showing the flux density at all available frequencies for a few selected dates along the outburst. From them, we can perform physical interpretation about which part of the system is radiating the most.

6.1 Motivation

If the flux density is proportional to a power of the frequency we have: $F_\nu \, \alpha \, \nu^\mu$, this assumes the spectrum can be described by a power law, which is a good approximation in a small wavelength range for typical emission processes like from the accretion disk and jet.

Thus, extracting logarithm in both terms, we end with: $\log F_\nu \, \alpha \, \mu \log \nu$. We call this μ as the spectral index and we want to test is if it changes across state transitions. In the next paragraphs we show that effectively μ is coupled to the state of the system.

6.2 Spectral Energy Distribution

First, we show the SEDs extracted from the TJO data for U, B, V, R, I bands. Then we combine in the same days the UVOT fluxes when available: 58321 (soft state), 58330 (soft state), 58413 (hard state) and 58436 (hard state), with a range of variability of 1 day in all cases, this is important because in the TJO observations the different filters cannot observe at the same time, so the MJD have discrepancies in the first decimal number. The data of MJD and de-reddened fluxes plotted are shown in Table 6.1: (the fluxes are in mJy units).

MJD	W2	M2	W1	U	B	V	R	I
58321 (IV)	21.60 ±1.30	27.99 ±1.85	28.06 ±1.49	28.65 ±1.27	26.20 ±1.04	28.15 ±1.24	22.64 ±2.27	20.30 ±2.59
58330 (IV)	33.30 ±2.07	33.66 ±2.22	32.82 ±1.74	35.40 ±1.57	27.66 ±1.10	30.13 ±1.32	24.74 ±2.48	20.30 ±2.59
58413 (VI)	5.04 ±1.20	8.14 ±0.54	7.95 ±0.45	9.00 ±0.08	8.75 ±0.35	10.79 ±0.48	9.56 ±0.96	9.83 ±1.26
58436 (VI)	2.87 ±0.18	2.72 ±0.19	2.81 ±0.16	3.38 ±0.15	3.00 ±0.13	2.88 ±0.13	1.64 ±0.17	2.75 ±0.35

Table 6.1. Fluxes (mJy) used to represent the different SEDs.

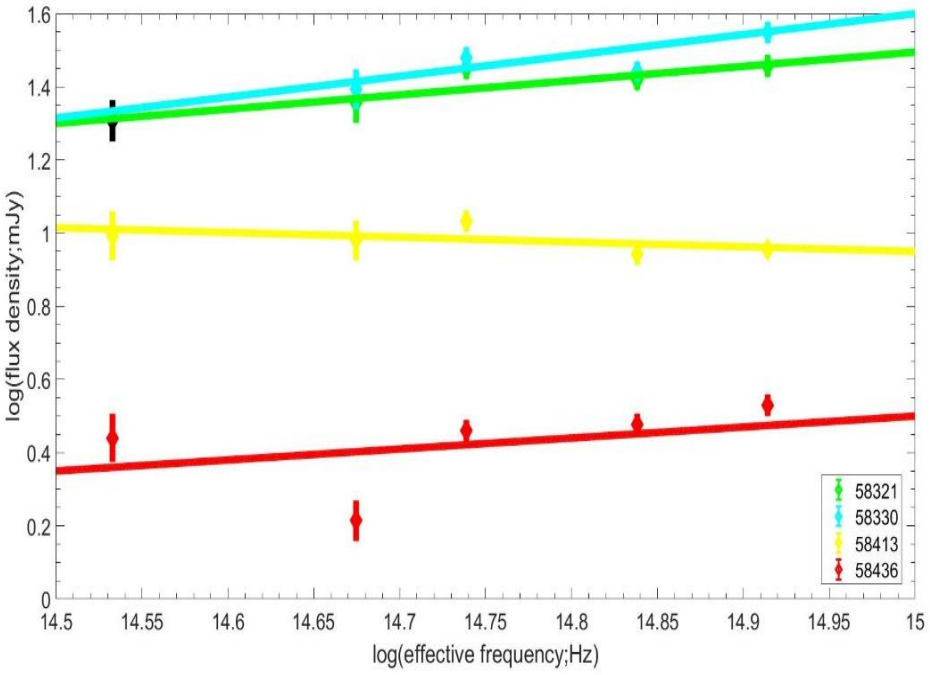

Figure 6.1. Linear fit TJO data (SED) previously extracting logarithm in both axes.The black point belongs simultaniosly to 58321 and 58330. Observe the slopes in the different states. The units are mJy for flux density and Hz for effective frequency.

To obtain the μ for each day we use polyfit task in Matlab. Polyfit fits a line to the flux values and returns the equation of a line, from it we can extract the slope (μ) polyfit also calculates the residual errors of the used data. As X axis, we use the effective frequency of each filter which can be obtained immediately with

$$c = \lambda_{eff} * \nu_{eff} \quad (6.1)$$

using the central wavelengths in Chapter 2. As Y axis, we use the de-reddened flux value shown in Table 6.1.

We may expect all the SED plots to fulfil a common pattern in the hard (μ≈0) and the soft (μ≈1) states. However, these μ values may encompass a large range of values, and in general the pattern expected is $\mu_{soft} > \mu_{hard}$. This answers the question that we asked before if state transitions affect the spectral index. This is clearly seen in the SEDs including the linear fit.

After that, we can add UVOT fluxes to the SEDs to check if there are substantially changes. We call this SED: broadband SED (B-SED).

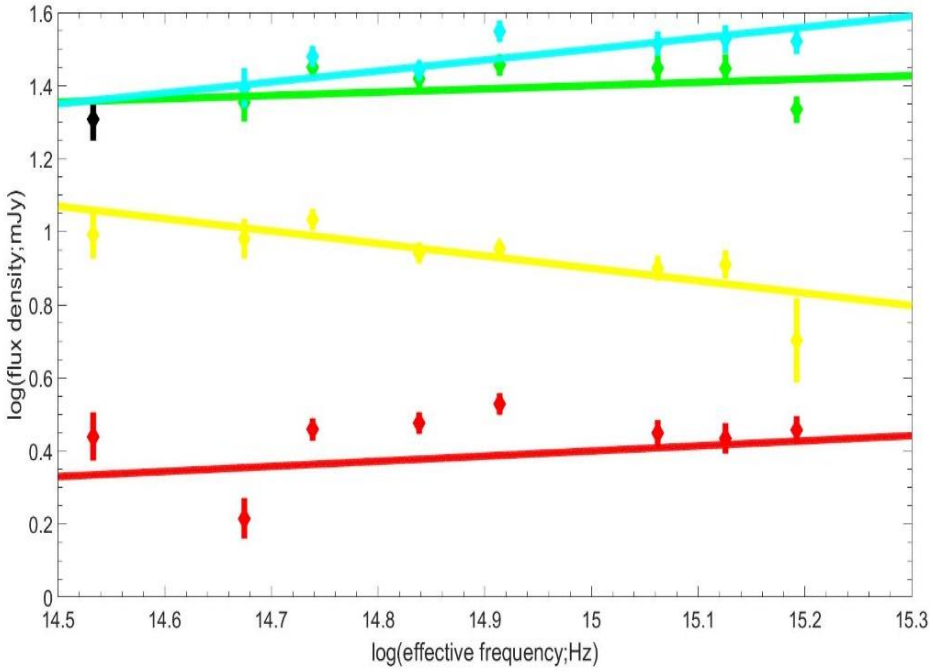

Figure 6.2. Linear fit using UVOT&TJO data (B-SED) previously extracting logarithm in both axes. The black point belongs simultaniosly to 58321 and 58330. Observe the slopes in the different states. The units are mJy for flux density and Hz for effective frequency.

Note that the plots are represented in a log-log scale. In which, the X-axis encompasses the 14.5-15 log scale of frequency (Hz) in SED and 14.5-15.3 in the B-SED and Y-axis of 0-1.6 log scale of flux density (mJy) in both cases.

MJD	State	Spectral Index SED	SED Residual Norm	Spectral Index Broadband SED	B-SED Residual Norm
58321	Soft	0.39	0.14	0.09	0.34
58330	Soft	0.57	0.16	0.30	0.26
58413	Hard	-0.12	0.14	-0.33	0.38
58436	Hard	0.38	0.49	0.14	0.53

Table 6.2. Different MJD and the spectral index obtained with TJO data and UVOT&TJO.

From the Table 6.2 we can conclude that the SED and B-SED agree with $\mu_{soft}>\mu_{hard}$ in all cases, except the last row compared to the first. In 58321, the spectral index 0.39 is reduced to 0.09. In 58330, the spectral index 0.57 is converted into 0.30 indicating that the broadband spectrum is harder. For 58413, the spectrum reduces from -0.12 to -0.33. Finally, in 58436 the index reduces from 0.38 to 0.14 as expected since in hard state we expect the spectral index become close to 0.

From these reasons and from the previous table (Table 6.2), we conclude that the spectral index in the TJO SED gives evidence that the emission is bluer in the soft than in the hard state. This can be attributed to the cooling of the outer parts of the disk (see Chapter 7).

Moreover, in the B-SED we are sampling an extended range of frequencies. B-SED does not show a clear pattern owing to in this extended range other components of the system which radiate in the near ultraviolet may be present. This results in a disordered appearance and supports our hypothesis of the multi-components system sampling.

To finish, we could say that this SED decomposition is more useful when considering optical wavelengths associated to U, B, V, R, I filters. This is because this system is dominated by disk radiation and it mostly lies on these wavelengths. When extending the range with higher frequencies, the B-SED collects the radiation of the hotter parts of the disk which might not be uniformly distributed. In addition, when adding more points to fit a line increases the error in the desired slope.

CHAPTER 7. Physical Interpretation and Conclusions

7.1 Physical Interpretation

In this section we give a physical interpretation of the results obtained in this project. We characterize the different states and attempt to give a physical interpretation to all MAXI J1820+070 data processed. We have seen soft, hard state profiles in X-ray emission and changes in the colours that we summarize to try to explain the behaviour of the system:

The two main results obtained are:

- The R-I colour increase in the soft state. Which we interpret as the disk cooling down during this state, the global temperature of the system diminishes.
- The bluer emission in the soft state in the optical range. This can be attributed to the cooler temperatures expected in the hard state. These cooler temperatures are occasioned by the lower luminosities (less flux) in this state, which cannot maintain the soft state system's temperature.

We suggest that the temperature during the soft state is governed by these two quantities. There are moments when the reprocessing is intense and an important quantity of X-rays reach the outer part of the disk, and others when the radiation is not so intense and the temperature decreases. This decreasing in the temperature is noticeable in the R-I colour increase.

We propose that most of the radiation comes from the disk, the jet and the corona may become outshone in the soft state. In the hard state the accretion disk is expected to become cooler, due to lower values of flux as the accretion rate is diminished and perhaps a jet can be ejected. Alternatively, the jet may be contributing to the optical emission in the hard state, at the lowest frequencies, and that may be responsible for the different SED spectral indices that we measure. A detailed physical multi-component modelling of the broad-band SED should be able to distinguish between these scenarios.

On the other hand, we associate the soft state with closer distance between the black hole and the inner part of the accretion disk; but we do not expect the jet to be present or to be outshone.

Another fact is that black hole accretion via an optically disk has been studied for decades and is known to produce reliable spectral predictions. This emission can be modelled as a multi-temperature blackbody type (Done 2002).

The information also given by the colours shown in TJO and UVOT results is susceptible to be physically interpreted. In order to relate this with the changes of the temperature we can rely on the reprocessing.

For example, in the R-I colour whose increase causes a diminution in the temperature we can relate that with the reprocessing. This occurs when photons, after receiving energy from inner hot electrons, collide with the outer parts of the accretion region such as the outer region of the disk or its wind. This causes a rise in the outer temperature, but always remaining several orders of magnitude below the inner part.

7.2 Conclusions

After all the exhaustive analysis done, we have extracted and interpreted all the MAXI J1820+070 information that our equipment has been able to give us. Our initial goal was to monitor the outburst of MAXI J1820+070. We have accomplished this objective obtaining the optical and UVOT light curves and giving a detailed description of the followed steps and software used. We have also with MAXI data focus on X-ray emission, to put us in situation of the states that a typical black hole transient follows.

With the information of the magnitude in the different filters, we have been able to convert these magnitudes into fluxes and obtain the spectral energy distribution in soft and hard states, detecting changes in the slope (spectral index) of the line that approaches its points.

Moreover, with the magnitudes we have been able to calculate the colour indexes. Useful parameters to give physical interpretation on which are the parts of the system that are producing most of the radiation. Also trying to understand why a magnitude in one band increases or decreases comparing with the others during the outburst evolution. Finally, we give a physical interpretation of the system's parameters obtained throughout the project.

After all, we have found that MAXI J1820+070 follows the typical trend of a BHT. Starting in hard state, then transition to soft state and the last part of the outburst returns to the hard state. We have also found correlation between hardness, optical colours in the soft state.

This project finally has led us to a two main results: the increase of the R-I colour in the soft state and the evidence to have bluer optical emission in the soft state.

References

[1]-Cristina Zurita, Jorge Casares, and Jesús Corral-Santana, New results on the study of transient X-rays binaries Spanish Astrophysics VII, Proceedings of the X Scientific Meeting of the Spanish Astronomical Society held on July 9 - 13, 2012, in Valencia, Spain.

[2]-Frank, J., King, A., & Raine, D. (2002). ACCRETION IN BINARY SYSTEMS. In Accretion Power in Astrophysics (pp. 48-79). Cambridge: Cambridge University Press. doi:10.1017/CBO9781139164245.007

[3]-Seward, F., & Charles, P. (2010). X-ray binaries. In *Exploring the X-ray Universe* (pp. 171-241). Cambridge: Cambridge University Press. doi:10.1017/CBO9780511781513.012

[4]-Jesus M. Corral-Santana, Jorge Casares, Teo Munoz-Darias, Franz E. Bauer, Ignacio G. Martinez-Pais, David M. Russell, BlackCAT: A catalogue of stellar-mass black holes in X-ray transients, October 2015.

[5]-Soleri,P. Accretion/Ejection Coupling in X-ray Binaries, PhD Thesis, UvA, 2010.

[6]-Casares,J. in *Ap&SS* Proc. (Springer,Berlin)The Physics of Accretion onto Black Holes,2010.

[7]-Gilfanov, M. 2010, in Lecture Notes in Physics, Berlin Springer Verlag, Vol.794, Lecture Notes in Physics, Berlin Springer Verlag, ed. T. Belloni, 17.

[8]-S. E. Motta, P. Casella, M. Henze, T. Muñoz-Darias, A. Sanna, R. Fender, T. Belloni, Geometrical constraints on the origin of timing signals from black holes, *Monthly Notices of the Royal Astronomical Society*, Volume 447, Issue 2, 21 February 2015, Pages 2059–2072.

[9]-T. Muñoz-Darias, S. Motta, H. Stiele, T. M. Belloni, The black hole candidate MAXI J1659−152: spectral and timing analysis during its 2010 outburst, *Monthly Notices of the Royal Astronomical Society*, Volume 415, Issue 1, 21 July 2011, Pages 292–300.

[10]-Kawamuro et al. 2018, MAXI/GSC detection of a probable new X-ray transient MAXI J1820+070, Astro Telegram ATel 11399.

[11]-Baglio et al. 2018, Optical observations of MAXI J1820+070 suggest it is a black hole X-ray binary, Astro Telegram ATel 11418.

[12]-Russell et al. 2006, *MNRAS*, 371, 1334; 2007, *Monthly Notices of the Royal Astronomical Society*, 379, 1108.

[13]-Baglio et al. 2019. Optical observations of MAXI J1820+070 confirm the rebrightening, Astro Telegram ATel 12596.

[14]-Zampieri et al. 2019 Optical observations of MAXI J1820+070 confirm the rebrightening, Astro Telegram ATel 12747.

[15]- Hambsch et al. 2019, Optical Rebrightening of ASASSN-18ey = MAXI J1820+070, Astro Telegram ATel 13014

[16]-T. Muñoz-Darias et al. 2016, Regulation of black-hole accretion by a disk wind during a violent outburst of V404 Cygni.Nature Publishing Group, a division of Macmillan Publishers Limited.

[17]-What's The Oadm - Institut d'Estudis Espacials de Catalunya. (2019). Retrieved from http://www.ieec.cat/en/content/206/what-s-the-oadm

[18]-Tawalbeh,Y et al. 2018. Modified Orbital Elements of The Close Visual Binary Systems Hip11352, Hip70973, and Hip72479.

[19]-Brauers, Johannes et al. "Multispectral Filter-Wheel Cameras: Geometric Distortion Model and Compensation Algorithms." *IEEE Transactions on Image Processing* 17 (2008): 2368-2380.

[20]- Fitzpatrick, E. (1999). Correcting for the Effects of Interstellar Extinction. *Publications Of The Astronomical Society Of The Pacific*, *111*(755), 63-75. doi: 10.1086/316293

[21]-Foight, D. R., Güver, T., Ozel, F., & Slane, P. O. 2016, *ApJ*, 826, 66.

[22]-Mathis et al. 1989. The relationship between infrared, optical, and ultraviolet extinction. Astrophysical Journal, Part 1 (ISSN 0004-637X), vol. 345, Oct. 1, 1989, p. 245-256.

[23]-Cohen, M., Walker, R., Barlow, M., & Deacon, J. (1992). Spectral irradiance calibration in the infrared. I - Ground-based and IRAS broadband calibrations. *The Astronomical Journal*, *104*, 1650. doi: 10.1086/116349

[24]-Homan et al. 2018.A rapid state transition in MAXI J1820+070. Astro Telegram ATel 11820.

[25]-S.E.Motta et al. 2018, Swift observes MAXI J1820+070 in transition from the soft to the hard-intermediate state. Astro Telegram ATel 12064.

[26]-Hynes, R. I. 2005. The optical and ultraviolet spectral energy distributions of short-period black hole X-ray transients in outburst. *ApJ*, 623, 1026–1043

[27]-Sjoert van Velzen and Heino Falcke, the contribution of spin to jet-disk coupling in black holes, *A&A*, 557 (2013) L7

[28]-Done, Accretion Flows in X-ray Binaries, *Philosophical Transactions of the Royal Society* (Series A: Mathematical, Physical, and Engineering Sciences), 2002.

Acknowledgements

It has been such a pleasant experience for me to take part on this project and have learnt about X-ray binaries and the methods used to study them. Since this project has been done in Barcelona and in Abu Dhabi, several people have helped in its progress.

First, I have to say that going to Abu Dhabi has been a very rewarding experience for me and I would like to thank Astrophysics Group in New York University Abu Dhabi for the financial aid supplied.

I am very grateful to my both advisors Manu Linares & Dave Russell, for their implication, useful advice throughout the project since their exceptional knowledge in binary systems and for their friendly attitude towards me. I have learnt a lot of physics (and English) from them.

I would like to mention Yago Herrera, my office mate in Barcelona who helped me with programming tasks. When in Abu Dhabi, Cristina Baglio contributed to the project helping with magnitude calibration.

And finally, I wish to thank to my family and friends that have always been there during these years of study.